ACS NANO
Cite This: ACS Nano 2019, 13, 10520−10534
www.acsnano.org

ARTICLE

How Substitutional Point Defects in Two-Dimensional WS_2 Induce Charge Localization, Spin−Orbit Splitting, and Strain

Bruno Schuler,[*,†] Jun-Ho Lee,[*,†,‡] Christoph Kastl,[†,¶] Katherine A. Cochrane,[†] Christopher T. Chen,[†] Sivan Refaely-Abramson,[†,▲] Shengjun Yuan,[§] Edo van Veen,[∥] Rafael Roldán,[⊥] Nicholas J. Borys,[#] Roland J. Koch,[□] Shaul Aloni,[†] Adam M. Schwartzberg,[†] D. Frank Ogletree,[†] Jeffrey B. Neaton,[*,†,‡,■] and Alexander Weber-Bargioni[†]

[†]Molecular Foundry, Lawrence Berkeley National Laboratory, Berkeley, California 94720, United States
[‡]Department of Physics, University of California at Berkeley, Berkeley, California 94720, United States
[¶]Walter-Schottky-Institut and Physik-Department, Technical University of Munich, Garching 85748, Germany
[§]Key Laboratory of Artificial Micro- and Nano-structures of Ministry of Education and School of Physics and Technology, Wuhan University, Wuhan 430072, China
[∥]Radboud University of Nijmegen, Institute for Molecules and Materials, Heijendaalseweg 135, 6525 AJ, Nijmegen, The Netherlands
[⊥]Instituto de Ciencia de Materiales de Madrid, ICMM-CSIC, Cantoblanco, E-28049, Madrid, Spain
[#]Department of Physics, Montana State University, Bozeman, Montana 59717, United States
[□]Advanced Light Source, Lawrence Berkeley National Laboratory, Berkeley, California 94720, United States
[■]Kavli Energy Nanosciences Institute at Berkeley, Berkeley, California 94720, United States
[▲]Department of Materials and Interfaces, Weizmann Institute of Science, Rehovot 7610001, Israel

Supporting Information

ABSTRACT: Control of impurity concentrations in semiconducting materials is essential to device technology. Because of their intrinsic confinement, the properties of two-dimensional semiconductors such as transition metal dichalcogenides (TMDs) are more sensitive to defects than traditional bulk materials. The technological adoption of TMDs is dependent on the mitigation of deleterious defects and guided incorporation of functional foreign atoms. The first step toward impurity control is the identification of defects and assessment of their electronic properties. Here, we present a comprehensive study of point defects in monolayer tungsten disulfide (WS_2) grown by chemical vapor deposition using scanning tunneling microscopy/spectroscopy, CO-tip noncontact atomic force microscopy, Kelvin probe force spectroscopy, density functional theory, and tight-binding calculations. We observe four different substitutional defects: chromium (Cr_W) and molybdenum (Mo_W) at a tungsten site, oxygen at sulfur sites in both top and bottom layers (O_S top/bottom), and two negatively charged defects (CD type I and CD type II). Their electronic fingerprints unambiguously corroborate the defect assignment and reveal the presence or absence of in-gap defect states. Cr_W forms three deep unoccupied defect states, two of which arise from spin−orbit splitting. The formation of such localized trap states for Cr_W differs from the Mo_W case and can be explained by their different d shell energetics and local strain, which we directly measured. Utilizing a tight-binding model the electronic spectra of the isolectronic substitutions O_S and Cr_W are mimicked in the limit of a zero hopping term and infinite on-site energy at a S and W site, respectively. The abundant CDs are negatively charged, which leads to a significant band bending around the defect and a local increase of the contact potential difference. In addition, CD-rich domains larger than 100 nm are observed, causing a work function increase of 1.1 V. While most defects are electronically isolated, we also observed hybrid states formed between Cr_W dimers. The important role of charge localization, spin−orbit coupling, and strain for the formation of deep defect states observed at substitutional defects in WS_2 as reported here will guide future efforts of targeted defect engineering and doping of TMDs.

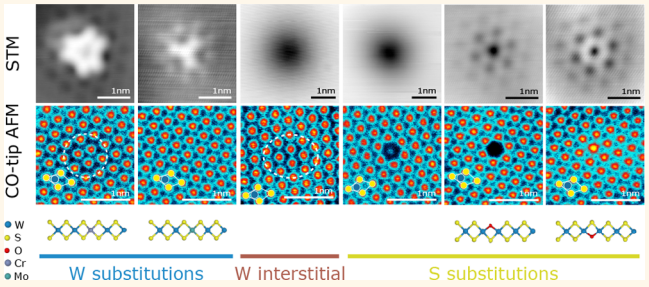

KEYWORDS: *point defects, 2D materials, transition metal dichalcogenide, WS_2, noncontact atomic force microscopy (nc-AFM), density functional theory (DFT), tight binding*

The introduction of impurity atoms in semiconductor crystals dramatically changes their conductivity, carrier mobility, and carrier lifetimes, among many other

Received: June 12, 2019
Accepted: August 8, 2019
Published: August 8, 2019

DOI: 10.1021/acsnano.9b04611
ACS Nano 2019, 13, 10520−10534

properties down to impurity concentrations at the parts per billion level. This extreme sensitivity to impurities required developing effective purification methods and strategies to mitigate the impact of defects, for instance by passivation, and to establish precisely controlled introduction of dopants, the foundation of modern semiconductor technology. Today, similar challenges are faced in two-dimensional (2D) materials science. Because of their intrinsic electron confinement, 2D materials are even more susceptible to structural defects.[1] Anticipating which defects or impurities are introduced during synthesis is often impossible given the complexity of reaction pathways and environmental variables. Moreover, predicting defect functionality, particularly for highly correlated materials, is far from trivial even with today's advanced theoretical methods and computational power. Identifying defects experimentally and probing their electronic structure is equally challenging, as it requires correlating the defect's atomic and electronic structure with atomic precision and milli-electronvolt energy resolution.

Monolayer transition metal dichalcogenides (TMDs)[2,3] are a remarkable class of 2D materials in several ways. Many are semiconducting (depending on composition and structure) with a direct band gap in the visible or near-infrared range, making them attractive for optoelectronic applications.[4] They are synthesizable by several established methods [chemical vapor deposition (CVD), metal organic chemical vapor deposition (MOCVD), atomic layer deposition (ALD), and molecular beam epitaxy (MBE)].[5] They exhibit strong light−matter interactions,[6] unique photophysics,[7,8] strong spin−orbit coupling,[9] and prominent many-body effects due to enhanced Coulomb interactions,[10,11] exemplified by the hundredfold enhancement of exciton binding energies as compared to bulk semiconductors.[12]

Tuning electronic, optical, and catalytic properties of 2D materials by means of defect engineering, in particular chemical doping, is a highly anticipated technology in the field.[1] In bulk semiconductors, shallow donor or acceptor states are typically used to control the carrier concentration. In 2D semiconductors, quantum confinement and screening effects generally lead to deeper defect energy levels and increasing defect ionization energies.[13] On the one hand, this limits the attainable free charge carrier concentration by chemical doping.[13] On the other hand, surface-bound deep defect levels are an ideal system for designing single-photon emitters[14,15] and catalysts.[1]

Structural defects such as domain boundaries,[16−18] dislocations,[18,19] vacancies,[16,18,20−22] interstitial atoms,[18] antisite defects,[16,18] and impurities[18,20,21,23−25] have been previously identified in TMDs and studied theoretically.[26−34] Such defects are believed to modify charge transport,[35] to host defect-bound excitons,[36−39] and to act as single-photon quantum emitters.[15,40−43] It is also suspected that point defects represent active sites in catalytic processes on the otherwise inert TMD surface.[44−46] In light of these anticipated functionalities there are growing efforts toward targeted incorporation of substitutional defects for doping and alloying of TMDs to tune their electronic, magnetic, optical, and catalytic properties.[18,47−50]

Establishing structure−function relationships for such defects or dopants is, however, challenging. Often macro- or mesoscopic ensemble measurements are correlated with atomic-resolution microscopy techniques to infer a certain defect functionality. The presence or prevalence of a certain defect does not necessarily indicate causality of the observed property. Instead, electronic and optical properties need to be measured locally to establish an unambiguous link to a specific structural defect. Moreover, two major complications impede defect identification itself by using the two prime experimental methods, aberration-corrected transmission electron microscopy (AC-TEM) and scanning tunneling microscopy (STM). First, TMDs are electron beam sensitive, which can cause *in situ* generation of defects—in particular chalcogen vacancies—by TEM.[16,18,20,30,35,51] Second, identification of defect atomic structure by STM is very challenging because the STM contrast is dominated by electronic effects, which has led to contradictory defect assignments by STM-only studies.[52−54] Both of these complications have supported the notion that chalcogen vacancy defects are abundant in as-grown TMDs under ambient conditions, which we have recently challenged.[22,25] We showed that oxygen substituting sulfur is the most abundant point defect in CVD-grown WS_2,[25] and chalcogen vacancies, which are absent in as-grown samples, can be created by high-temperature annealing under vacuum.[22]

Here, we report the direct correlation of the atomic and electronic structure of commonly observed point defects in CVD-grown monolayer WS_2 samples using a combination of low-temperature scanning tunneling microscopy/spectroscopy (STM/STS), CO-tip noncontact atomic force microscopy (nc-AFM), Kelvin probe force spectroscopy (KPFS), density functional theory (DFT), and tight-binding calculations. Six point defects occurring in as-grown samples were found and investigated. Four of them were identified as W or S substitutions: Cr_W (chromium substituting tungsten), Mo_W (molybdenum substituting tungsten), and O_S (oxygen substituting sulfur) in the top and bottom sulfur layer. In addition, we observed two types of negatively charged defects (CDs), where the impurity atom could not be unambiguously identified.

We discuss in detail the electronic defect states associated with each of these defects. Particularly the roles of spin−orbit coupling, crystal-field splitting, and strain are analyzed, and the origin of the qualitatively different behavior of isoelectronic substituents is examined. One case of defect state hybridization is discussed. Furthermore, the negative charge localization at two types of defects is demonstrated, which induces significant local band bending and a dramatically higher work function of mesoscopic CD-rich domains.

These results advance our understanding of the role of defects in TMDs. Unambiguous chemical assignment of defects suggests formation pathways, optimized synthetic processes, and routes to controlled chemical doping. Detailed structural and electronic characterization provides insights into underlying fundamental physical principles. Of particular interest is the observation of spin−orbit split deep in-gap states for Cr_W and the annealing-induced sulfur vacancy as well as the defect-bound charge at both CDs. The latter can be expected to form bound trions, scatter charge carriers, and act as an efficient recombination site, while the former are potential candidates for single-photon emitters.

RESULTS AND DISCUSSION

Monolayer WS_2 was grown using a CVD process on epitaxial graphene (Gr) on SiC(0001).[55−57] The tungsten oxide ($WO_{2.9}$) powder and H_2S gas precursor streams were compartmentalized to prevent sulfurization of the transition metal oxide precursor during growth.[57,58] More details on the sample growth and preparation prior to low-temperature scanning probe inspection can be found in the Methods section and ref 57. The Gr/SiC substrate only weakly interacts with the WS_2 layer, preserving its

DOI: 10.1021/acsnano.9b04611
ACS Nano 2019, 13, 10520−10534

interesting intrinsic band structure, such as the direct band gap in the visible range and the spin−orbit splitting at the K-point.[56,57] The most notable exception is a substrate-induced pinning of the WS_2 Fermi level to the upper third of the band gap, near the conduction band edge.[56,59] The reported values of the substrate-induced doping vary between different studies, most likely as a consequence of varying growth conditions, which can affect the interfacial states of the graphene/buffer layer system, for instance through intercalation.[60] Also, the quasiparticle band gap becomes smaller with increasing number of graphene layers due to the increased substrate screening (see Supporting Information).[10]

Figure 1a shows a 3D representation of an STM overview image of a monolayer WS_2 island on Gr/SiC. The island edges (indicated by the dashed line) are usually not clearly faceted and appear to be decorated with adsorbates, but were recently also associated with air-induced oxidation of the edges.[61] By contrast, the inside of the island is clean and a variety of point defects can be discerned. The relative frequency of different defects and the overall defect density vary considerably between different samples, but both usually do not depend on the location on the sample or the number of repetitions of low-temperature (250 °C) vacuum annealing steps. The type of defects that are created will also depend on the synthetic conditions (such as the precursor material) and hence might vary for different growth methods. The defect density summed over all occurring defects in our samples is typically on the order of 10^{12} cm^{-2}, and the defects are randomly distributed. An exception is a charged defect species, where segregated CD-rich domains were found (see the section Work Function Change at CD-Rich Domains). In the two close-up images (Figure 1b,c) five types of defects can be distinguished. Their characteristic STM topography is voltage and tip termination dependent. Here, we chose a sample bias of 1.1 V, which is about 200 mV above the WS_2 conduction band edge where the contrast difference is most apparent. In addition, a CO-terminated tip was used for enhanced resolution.[62,63] The two types of charged defects can, however, not be distinguished under these scanning conditions. All discussed defects, except for the CDs, have a 3-fold symmetry indicative of the trigonal prismatic lattice of the host crystal. In fact, the defect's STM contrast can be used to determine the full lattice orientation, which is particularly helpful to identify 60° grain boundaries. A defect assignment by STM is, however, very challenging without *a priori* knowledge of their origin, *e.g.*, by deliberate incorporation of a specific impurity by synthetic means. Even assigning the lattice site is not trivial given that tip- and bias-dependent contrast inversions have been observed.[64,65] These complications have led to contradictory defect assignments and have in particular supported the conception that chalcogen vacancy defects are abundant in TMDs under ambient conditions, which we could refute in two recent publications.[22,25]

WS_2 Defect Assignment and Electronic Fingerprint. Here, we employ a combination of STM/STS, CO-tip nc-AFM, and DFT to provide a comprehensive characterization of all commonly observed defects in our CVD-grown monolayer WS_2: Cr_W, Mo_W, O_S in the top and bottom sulfur sublattice and two charged defects (CD type I and CD type II). In Figure 2a−f and Figure 2i−n STM topography images and the corresponding CO-tip nc-AFM images of the six WS_2 defects are shown, which we find in our CVD-grown samples. A model of our defect assignment is provided in Figure 2q−t and will be justified later in this section. Based on the well-established contrast

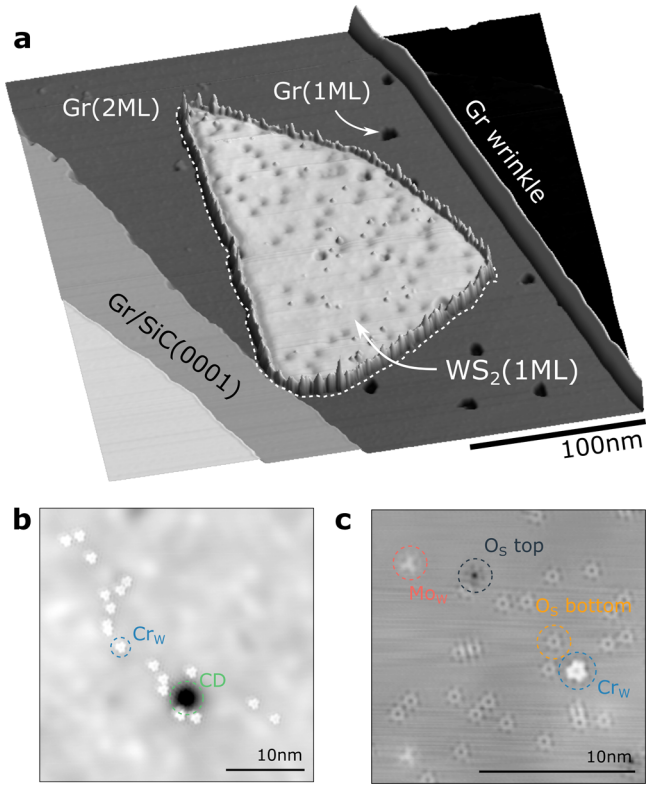

Figure 1. Monolayer WS_2/Gr/SiC sample. (a) Pseudo 3D STM topography of a WS_2 island on Gr/SiC. (b,c) STM images (I = 20 pA, V = 1.1 V) of single defects on WS_2. One of each defect type is labeled.

mechanism of CO-tip nc-AFM,[62,66,67] the surface-layer S atoms and the lower-lying W atoms can be recognized as the circular bright and dark features in Figure 2i−p, which define the unit cell of 1H-WS_2 as indicated in the lower left corner of each panel. Assigning the W positions in the subsurface layer is important to distinguish between W substitutions and interstitial defects. The two rightmost columns in Figure 2 depict sulfur vacancies in the top and bottom sulfur sublattice for comparison. These sulfur vacancies are *not* found in as-grown samples but could be created by high-temperature annealing in vacuum.[22] The identification and characterization of the abundant oxygen substituent O_S as well as the annealing-induced sulfur vacancy Vac_S are discussed in detail in refs 25 and 22, respectively. In short, the oxygen substituent at a sulfur site only marginally affects the WS_2 electronic properties; in particular it does not introduce defect states in the band gap.[25] On the other hand, sulfur vacancies that were created by annealing under vacuum at 600 °C feature two sharp unoccupied in-gap defect states followed by vibronic satellite peaks in STS. Most importantly, the 252 meV energy splitting between the two defect states results from a strong spin−orbit interaction.[22] The oxygen substitution efficiently passivates the sulfur vacancy by removing its deep in-gap defect states.

In the following, we present the unambiguous identification of Cr_W and Mo_W based on their nc-AFM contrast and electronic fingerprint and provide a detailed characterization of the two charged defects, which introduce significant band bending.

Chromium Substituting Tungsten (Cr_W). The defect assigned as Cr_W (chromium substituting tungsten) (Figure 2i) is located at a W site, evident by a faint nc-AFM contrast that includes the neighboring three sulfur atoms (within encircled

DOI: 10.1021/acsnano.9b04611
ACS Nano 2019, 13, 10520−10534

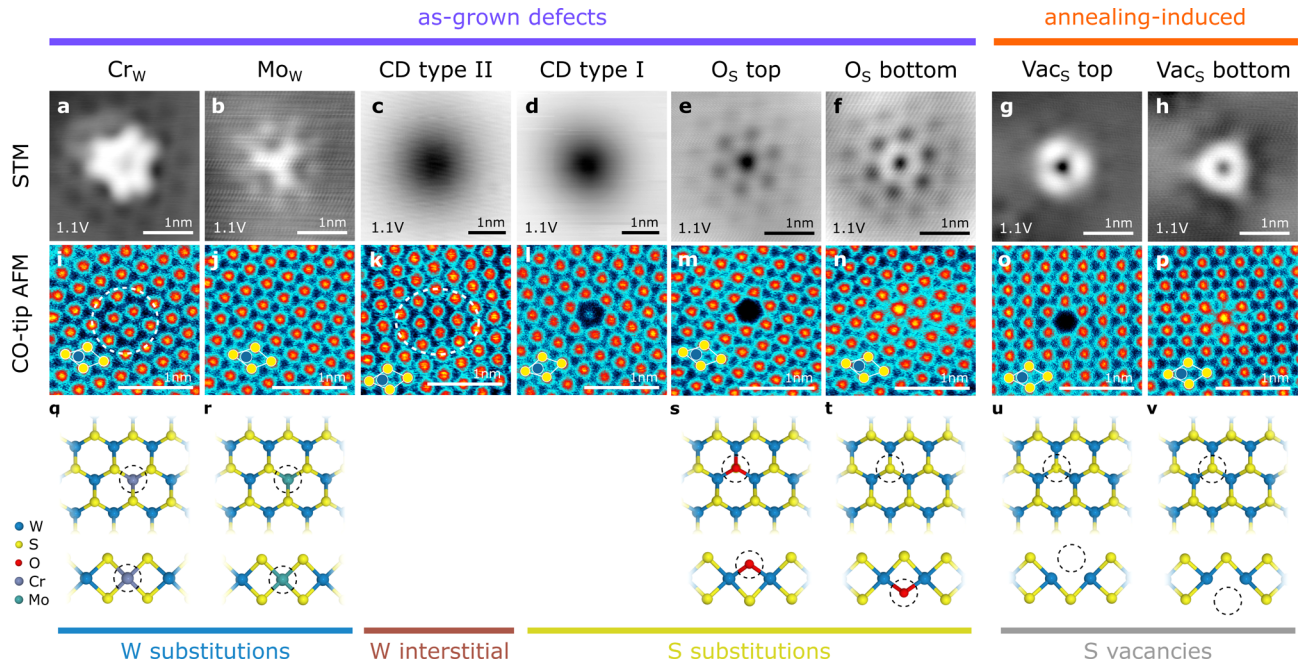

Figure 2. Point defects in WS_2. (a–f) STM topography of the defects observed in as-grown CVD-WS_2: Cr_W (a), Mo_W (b), CD type I and II (c, d), and O_S top/bottom (e, f), respectively. (g,h) STM topography of annealing-induced S vacancies Vac_S top/bottom. (i–p) Corresponding CO-tip AFM image of the same defects. The S and W atoms are indicated by the yellow and blue disks. The white rhombus defines the unit cell of the 1H-WS_2 island. In i and k the defect location is marked by the dashed circle as a guide to the eye. (q–v) Top and side view of the DFT-calculated atomic defect structure. Defect locations are marked by a circle.

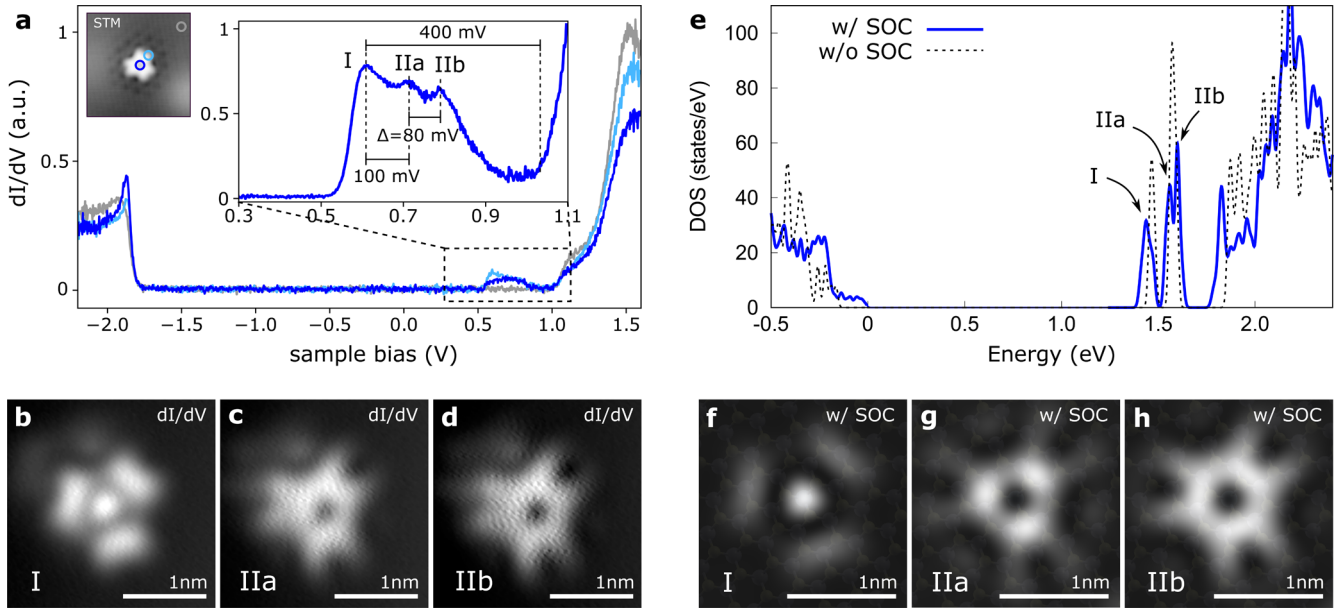

Figure 3. Defect states of Cr substituent at W site (Cr_W). (a) STS measurements of a Cr_W defect showing three distinct in-gap states. The circles in the inset STM image indicate the spectra positions. The lowest defect state I is 400 mV below the conduction band edge and separated by 100 and 180 mV from the two consecutive defect orbitals (IIa and IIb). (b–d) Experimental dI/dV maps of the three Cr_W defect states. Note that the defect orbitals IIa and IIb in c and d closely resemble each other. (e) Calculated density of states (DOS) of WS_2 containing a Cr substituent without (dashed line) and with (blue line) SOC using DFT-PBE (see Methods). The valence band maximum of the DOS with SOC is set to zero energy, and the DOS without SOC is aligned such that the defect state at higher energy is located in the center of the IIa and IIb states. (f–h) Integrated local density of states for the three Cr_W defect states in a 7 × 7 supercell.

region). The observed contrast is in excellent agreement with nc-AFM simulations of a Cr substituent based on the probe particle model[67,68] (see Figure S6 in the Supporting Information). In particular, the experimentally observed inward relaxation of the closest surface S atoms by 0.14 Å is quantitatively reproduced by our DFT calculations. The effect of the resulting lattice strain will be discussed in the section Isoelectronic Trap States Due to *d* Shell Energetics and Strain: Cr_W *vs* Mo_W. The CO-tip nc-AFM contrast is, however, not unique to Cr_W. A similar contrast is expected for V_W (vanadium

DOI: 10.1021/acsnano.9b04611
ACS Nano 2019, 13, 10520–10534

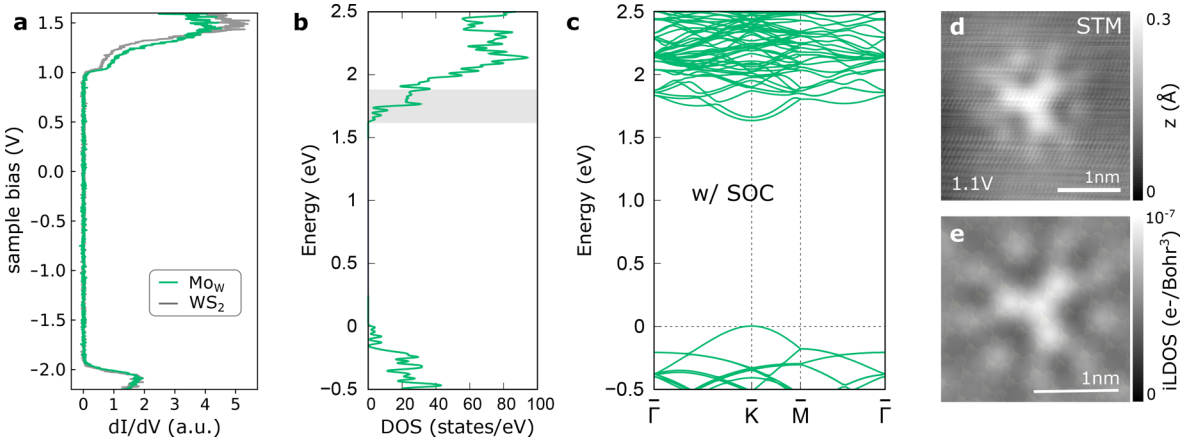

Figure 4. Electronic signature of a Mo substituent at the W site (Mo_W). (a) dI/dV spectrum on a Mo_W defect (green) and bare WS_2 (gray). (b) Calculated DOS with DFT-PBE-SOC of WS_2 with a Mo substituent. The valence band maximum is set to zero in energy. (c) Corresponding band structure of Mo_W. (d) STM topography of Mo_W at 1.1 V. (e) Integrated local density of states for a Mo_W defect. The integrated energy range is marked by the gray box in b.

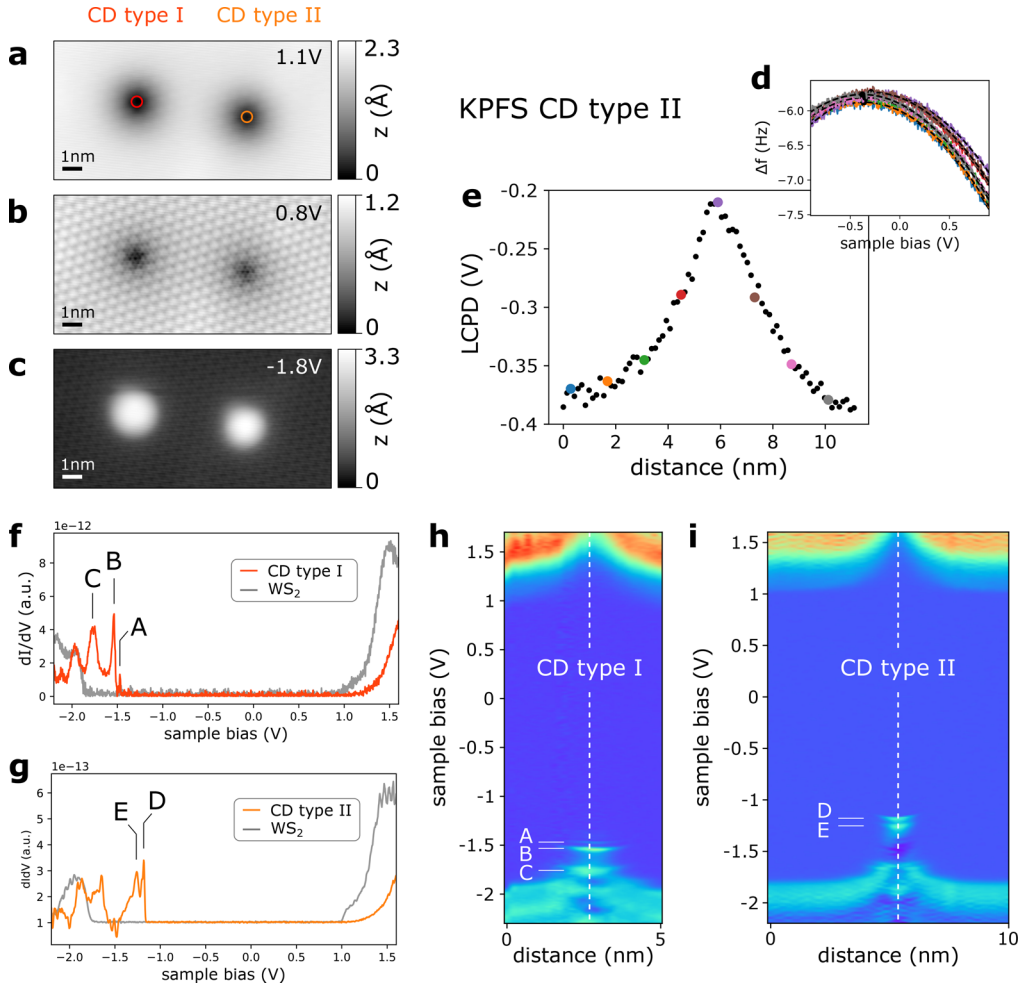

Figure 5. Charged defect (CD) type I and CD type II. (a–c) STM topography of the two charged defects, CD type I (left) and CD type II (right). Both appear as a large depression at positive sample bias and a large protrusion at negative bias. (d) Kelvin probe force spectroscopy (KPFS) parabola measured across a CD type II defect. (e) Extracted local contact potential difference (LCPD) from the vertex points in d. The colored points correspond to the subset of parabolas shown in d. The greater LCPD at the CD defect indicates negative charge. (f) dI/dV spectrum on a CD type I (red) and on the pristine WS_2 (gray). Three major resonances at negative sample bias are labeled A–C. (g) dI/dV spectrum on a CD type II (orange) and on the pristine WS_2 (gray). Two major resonances at negative sample bias are labeled D and E. (h, i) dI/dV spectra taken across CD type I and CD type II, respectively. The lateral defect positions are indicated by the vertical dashed lines. For both types of defects a clear upward band bending and occupied defect resonances are observed.

DOI: 10.1021/acsnano.9b04611
ACS Nano 2019, 13, 10520–10534

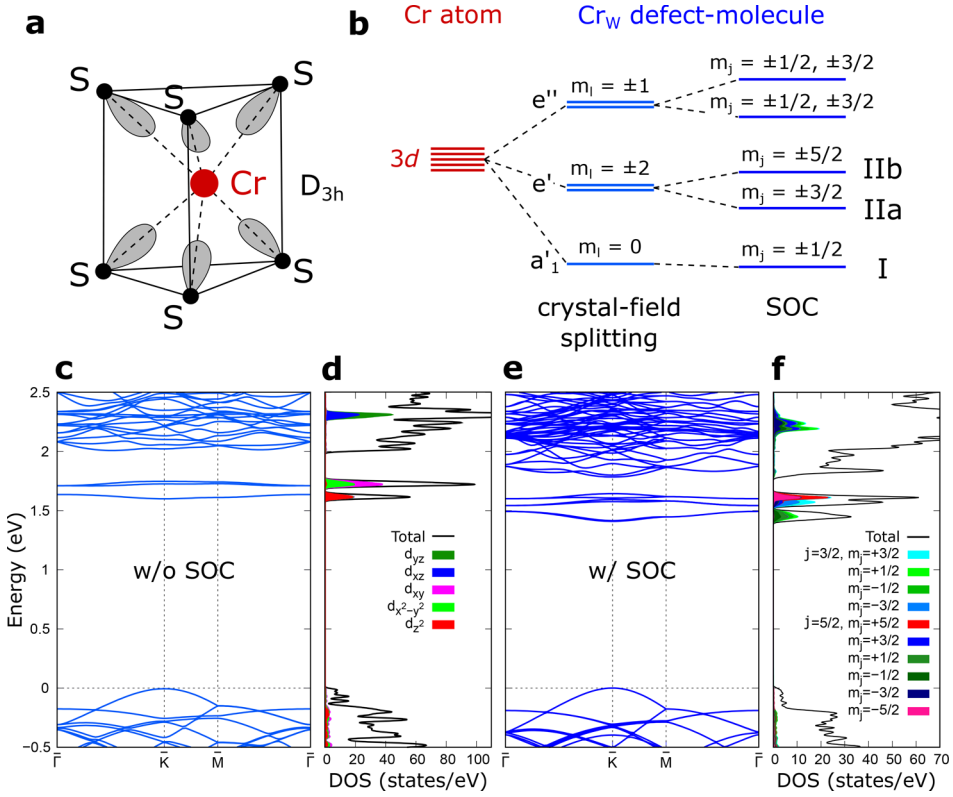

Figure 6. Orbital splitting of Cr_W defect states. (a) Schematic of a Cr atom in a trigonal prismatic (D_{3h}) "ligand" field created by six neighboring S atoms. (b) Energy level diagram (not to scale) of the "defect−molecule" model highlighting the lifting of Cr's d orbital degeneracy by the crystal field and SOC. a_1', e′, and e″ denoted the irreducible representations of the D_{3h} point symmetry group. m_l and m_j refer to the eigenstates of $\hat{L}_z$ and $\hat{J}_z$, respectively. (c) Band structure of WS_2 with a Cr substituent without SOC. The valence band maximum is set to zero in energy. (d) Projected density of states on the Cr atomic d orbitals computed with DFT-PBE. The colored area is proportional to the contribution of each d orbital. (e) Band structure of WS_2 with a Cr substituent with DFT-PBE-SOC. (f) Projected density of states onto eigenstates of the total angular momentum operator $\hat{J}$ labeled with the main and secondary total angular momentum quantum numbers j and m_j, respectively.

substituting tungsten), Mn_W (manganese substituting tungsten), O_W, and S_W (see Figure S7). However, the defect's electronic signature unambiguously identifies it as Cr_W as discussed below.

The chromium substituent can be readily observed in the STM topography as a 3-fold symmetric protrusion when tunneling into unoccupied states at positive sample bias (see Figure 1b,c and Figure 2a). In Figure 3a, a differential conductance (dI/dV) spectrum of a Cr_W is shown, revealing three distinct defect resonances at 400 mV (denoted I), 300 mV (denoted IIa), and 220 mV (denoted IIb) below the conduction band minimum. These resonances are indicative of localized unoccupied defect states. dI/dV images at these resonance energies displayed in Figure 3b−d map out the corresponding defect states with a spatial extent of about 1 nm. Intriguingly, the two defect states at higher energies (denoted IIa and IIb) appear very similar, indicating a lifted orbital degeneracy.

The calculated DFT density of states for a Cr substituent (Figure 3e) and the shape of its associated defect orbitals (Figure 3f−h) closely resemble the experimental findings (see Methods for details of our calculations). The close correspondence of experiment and theory corroborates our defect assignment as Cr_W. Other possible candidates such as V or Mn substituents can be ruled out, as the former does not exhibit any in-gap state, and the defect states of the latter are distinctively different from experiment (see Figure S13).

By comparing DFT calculations with and without spin−orbit coupling (solid blue and dashed gray line in Figure 3e, respectively) we find that the $\Delta \approx 48$ meV splitting between IIa and IIb is a consequence of the spin−orbit interaction. This effect will be further discussed in the section Spin-Orbit Splitting of Cr_W Detect States.

Cr substituents in CVD-grown MoS_2 on SiO_2 have recently also been detected by single-atom electron energy loss spectroscopy,[69] suggesting that this substitutional transition metal atom is stable under electron irradiation and common in TMD samples.

Molybdenum Substituting Tungsten (Mo_W). Substituting a tungsten atom by molybdenum (Mo_W) only minimally affects the WS_2 lattice and electronic properties. In fact, Mo_W does not create a detectable contrast in nc-AFM (see Figure 2j). The lattice site could only be assigned by using close-by defects as atomic markers. In this way, we could relate the center of the defect observed in STM to the W sublattice (see Figure S3). There is also no significant modification of the WS_2 electronic spectrum evident in the dI/dV spectrum in Figure 4a.

The minimal effect on both the atomic and electronic structure confirms that the impurity atom is chemically similar to tungsten. Our DFT calculations indicate that indeed Mo is a likely candidate for several reasons. First, unlike the Cr_W case, the host crystal lattice does not significantly distort around a Mo_W impurity. The calculated in-plane sulfur−sulfur distance of the three neighboring surface S atoms only increases by 3 pm (1%), whereas we find a significant contraction of 14 pm (4.5%) for Cr (see Figure 8). Second, the DFT band structure of WS_2 with a Mo impurity, shown in Figure 4c, closely resembles the

DOI: 10.1021/acsnano.9b04611
ACS Nano 2019, 13, 10520−10534

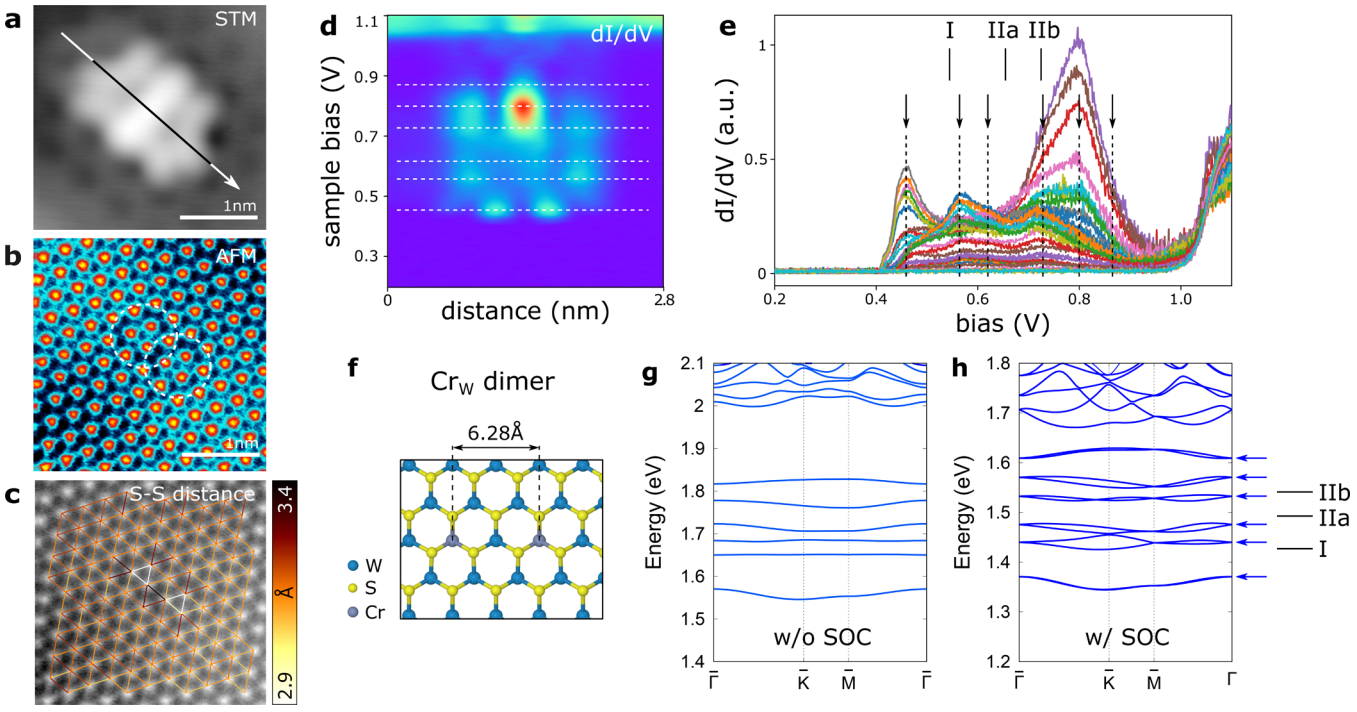

Figure 7. Hybrid states of a Cr_W dimer. (a) STM topography of a Cr_W dimer in the third-nearest-neighbor configuration. (b) CO-tip nc-AFM image of the same dimer. (c) Extracted S−S distance of the nc-AFM image shown in b revealing the local lattice strain. (d, e) dI/dV spectra recorded across the dimer (direction indicated by arrow in a). Six hybrid dimer states are marked by the dashed lines and arrows in e. The three single Cr_W states (I, IIa, IIb) are indicated for comparison. (f) DFT model of the same Cr_W dimer. (g, h) DFT band structure of the Cr_W dimer in a 7 × 7 supercell without (g) and with SOC (h). The six hybrid Cr_W dimer states are marked with blue arrows, and the three lines (I, IIa, IIb) indicate the calculated defect states of a single Cr_W for comparison.

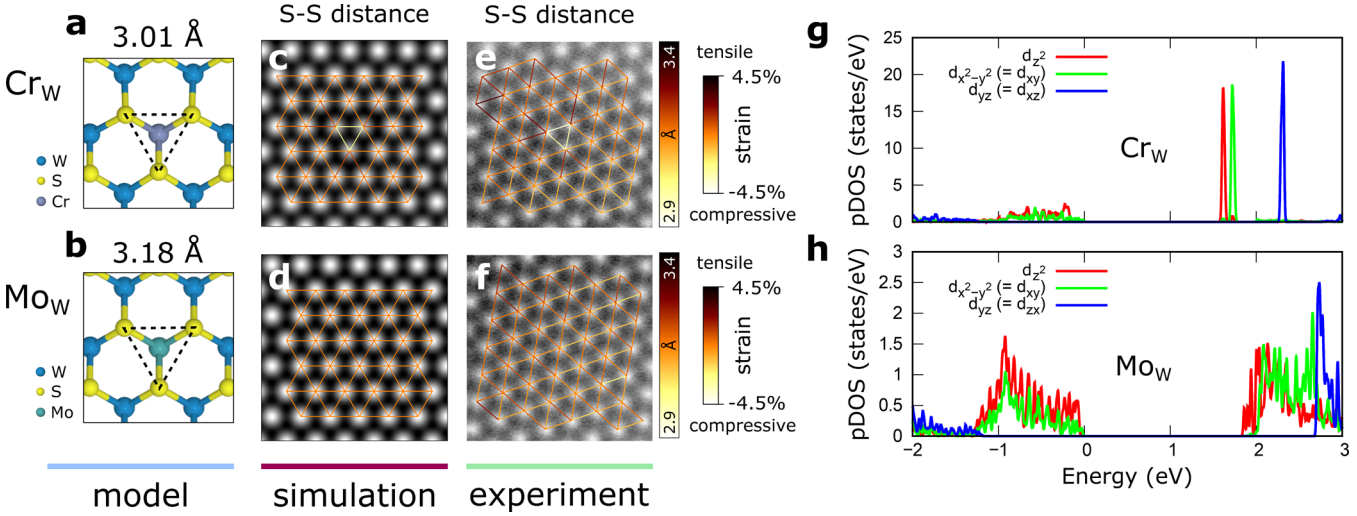

Figure 8. Cr_W *vs* Mo_W: strain and d orbital hybridization. (a, b) DFT-calculated relaxed defect geometry for Cr_W and Mo_W. The dashed lines indicate the sulfur−sulfur (S−S) distance in direct proximity of the substitute. This distance is considerably smaller (3.01 Å) for Cr_W as compared to perfect WS_2 (3.15 Å), indicating compressive strain. (c, d) Simulated CO-tip nc-AFM images based on the probe particle model[67,68] using the defect geometries shown in a and b. (e, f) Experimental CO-tip nc-AFM image of Cr_W and Mo_W. In c−f the atom positions have been determined using the Atomap[88] fitting routine, revealing the local strain around Cr_W and its absence around Mo_W in both the simulation and experiment. The % strain scale has been corrected for the CO tip tilting. (g, h) DFT-projected DOS onto Cr and Mo d orbitals showing the degree of hybridization.

band structure of pristine monolayer WS_2. Nonetheless, slight modulations of the local density of states lead to a characteristic shape observed in STM (Figure 4d) that is nicely reproduced by the DFT integrated local density of state (ILDOS) of Mo_W (Figure 4e), confirming our assignment.

We postulate that the source of the Cr and Mo is the $WO_{2.9}$ CVD precursor (99.99%, Alfa Aesar), which contains 1 ppm of Cr and 8 ppm Mo impurities (according to the certificate of analysis). A 1 ppm impurity concentration translates into a doping density of 2.3×10^9 cm^{-2}. Our observed impurity density of Cr_W and Mo_W is on the order of 10^{10} cm^{-2}, which is plausible

DOI: 10.1021/acsnano.9b04611
ACS Nano 2019, 13, 10520−10534

given that the evaporation and incorporation process of these species during CVD could be different from majority tungsten. In contrast to this dilute doping regime, other groups have deliberately synthesized ternary TMD alloys such as $Mo_{x-1}W_xS_2$[47] or $Mo_{x-1}W_xSe_2$[48,49] to continuously tune the band gap of TMDs.

Consistent with our experimental results, we find that Cr and Mo impurities at a tungsten site exhibit a much lower formation energy as compared to a sulfur or interstitial site. For Cr_W, a formation energy of 0.31 eV (W-rich limit) and 0.03 eV (S-rich limit) was calculated, whereas Cr_S yields 4.72 eV (W-rich limit) and 4.86 eV (S-rich limit) and Cr_i yields 6.70 eV. These values are obtained considering $WO_{2.9}$ and H_2S as the source of W and S, respectively. In the Supporting Information, more details on the calculation method of formation energies can be found. For Mo_W, Mo_S, and Mo_i we find a similar trend. This explains why only Cr_W and Mo_W are thermodynamically stable and frequently observed in our samples. We note that recent DFT calculations reveal that many transition metals at an interstitial site are energetically favorable in $MoTe_2$ where the in-plane lattice constant is ~11% larger as compared to WS_2.[70] In WS_2, the relatively small interatomic spacing renders interstitial atoms unfavorable. We also find that O impurities at sulfur sites have a significantly lower formation energy [0.54 eV (0.58 eV) for W-rich (S-rich) conditions] than a sulfur vacancy [1.53 eV (1.67 eV) for W-rich (S-rich) conditions], in line with our observations reported in refs 22 and 25.

Charged Defects Type I and Type II. The most easily observed but most difficult to identify defect in STM is what we refer to as the charged defect. In fact, we observed two types of charged defects, CD type I and CD type II. Both CDs appears as a large (~3 nm) depression at positive sample bias and a protrusion at negative bias (see Figure 5a–c). Similar STM contrast has been reported for synthetic MoS_2,[52] WSe_2,[54,71] $MoSe_2$[71] and natural bulk $MoS_2(0001)$.[72] Some of these reports propose that the observed defect is negatively charged[71,72] and speculate that it might be a subsurface defect[52] or chalcogen vacancy.[54] This apparent ambiguity in the literature reveals again the current lack of consensus on the assignment of TMD defects. The pronounced electronic STM contrast stems from band bending resulting from a trapped negative charge, as will be discussed below. In the section Work Function Change at CD-Rich Domains, the change in work function associated with CD-rich regions will be addressed.

Using Kelvin probe force spectroscopy, we could verify that both CDs are negatively charged. KPFS measures the local contact potential difference (LCPD) between tip and sample with sub-nanometer resolution[73] and single electron charge sensitivity.[74] The LCPD is determined by the vertex point of $\Delta f(V)$ parabolas.[74] As seen in Figure 5d,e, the LCPD shifts about 150 mV toward more positive bias above the CD defect, indicative of a net negative surface charge. In STS, CD type I (Figure 5f,h) and CD type II (Figure 5g,i) exhibit a complex electronic signature with several states above the valence band maximum. Characteristic for both CDs is the significant upward band bending of the conduction and valence band, as evident from dI/dV spectra across the defects shown in Figure 5h and i, respectively. This strong band bending observed within a few nanometers around the defect again suggests a negative charge trapped at the defect site. Presumably, an unoccupied acceptor state introduced by the defect gets filled from the graphene substrate, which is in tunneling contact and can exchange an integer amount of electrons. The Fermi level of graphene (0 V in dI/dV spectroscopy) dictates which defect levels are filled and which are empty. In addition, the charge state of a defect will be collectively determined by the Coulomb energy associated with the localized extra charge introduced into the system, the charge-induced lattice relaxations, and the screening by the TMD and graphene.

In Figure 5f–i we label the major resonances of CD type I with A–C and the major resonances of CD type II with D and E. These electronic resonances observed at CD defects can stem from either impurity states of the substituent or "hydrogenic" bound states in the screened Coulomb potential created by the excess negative charge.[75] The convolution of these two effects complicates the comparison to electronic defect states obtained by DFT, which is straightforward for neutral defects. In addition, orbital sequence reordering has been observed for charged molecular systems due to many-body interactions not captured by single-particle theories.[76,77]

Nevertheless we can narrow down possible CD type I and II defect candidates. The CO-tip nc-AFM image of CD type I shows that it is located at a sulfur site (see Figure 2l). The defect appears as a substituted atom in the top sulfur plane. Because we could remove the substituent by a voltage pulse with the tip, which left behind a sulfur top vacancy, we know that the CD type I defect does not include a modification of the bottom sulfur layer or the tungsten layer. Unlike O_S top, the substitution is clearly visible as a bright dot at the sulfur site. Two options are conceivable that would explain the observed contrast: (i) The defect could be a monatomic substitution that is less relaxed toward the tungsten plane as compared to an oxygen substituent, but lower in vertical distance than the sulfur plane. This characteristic is predicted for C_S and N_S. (ii) An alternative candidate is a diatomic substitution comprising a hydrogen atom, such as CH or NH. In that case, the hydrogen atom is above the sulfur plane, but because of its small electron density the AFM contrast is weak. In Figure S8 we compare simulated CO-tip nc-AFM images for CH_S, NH_S, C_S, N_S, and O_S. The best match is achieved for CH_S and NH_S.

In Figure S16 we also compare the DFT band structures of the five defect candidates mentioned above. We find that C_S and N_S form an unoccupied or half-occupied acceptor state, respectively. CH_S features a partially filled valence band and a resonant defect state. In all three cases, the formally unoccupied or partially occupied states are below the Fermi energy of the Gr/SiC substrate and are hence expected to be filled by the substrate. Therefore, based on the electronic spectrum, CH_S, C_S, and N_S are possible candidates that generate a bound negative charge like that observed at CD type I defects. NH_S and O_S have fully occupied bands and are expected to be neutral.

Nitrogen substitutions at sulfur sites have recently been detected by electron spin resonance in synthetic bulk MoS_2 samples.[78] This study found that such N substituents are very stable and act as p-type dopants, in line with our observations. Nitrogen dopants have also been deliberately introduced in MoS_2 and WS_2 using postgrowth treatment with nitrogen plasma.[79,80] Similarly, carbon–hydrogen (CH) units at sulfur sites could be introduced in WS_2 by a methane plasma-assisted process.[81]

The identification of CD type II is even more challenging since the CO-tip nc-AFM contrast is extremely faint, as shown in Figure 2k. By adjusting the contrast and color scale, a feature can be conjectured around a W interstitial and W site, which suggests that the defect is an off-centered W interstitial. This view is supported by correlating STM and AFM images (see

DOI: 10.1021/acsnano.9b04611
ACS Nano 2019, 13, 10520–10534

Figure S4) using an atomic O_S marker similar to the procedure applied for Mo_W, but with the complication that the CD STM contrast is less local. Therefore, this result comes with a higher degree of uncertainty. However, we can exclude that CD type II is a defect in the upper sulfur plane.

Spin−Orbit Splitting of Cr_W Defect States. Spin−orbit coupling (SOC) is a defining characteristic of the TMD band structure. The combination of SOC and lack of inversion symmetry of the TMD monolayer leads to spin-momentum locking at the K point of the Brillouin zone, the key element of valleytronic concepts.[8,82] The effect of SOC on defect electronic states has, however, not received much attention. Recently, we measured the spin−orbit splitting between WS_2 sulfur vacancy states.[22] The exceptionally large splitting (Δ = 252 mV), in that case, is due to the W 5d electrons that contribute to the vacancy states.

For Cr_W we observe a similar effect. For Cr_W's three in-gap defect states two arise from SOC, with a splitting of Δ = 80 mV [*cf.* the section Chromium Substituting Tungsten (Cr_W)]. In a simple atomistic picture the transition metal substitution can be regarded as an atom in an effective ligand field formed by the neighboring six sulfur atoms analogue to a coordination complex (see Figure 6a). This notion was introduced in the defect−molecule model by Coulson and Kearsley to describe color centers in diamond.[83] In this framework, the defect system is decoupled from the host lattice and molecular orbital theory can be applied. This approach is adequate for deep level defect states that are highly localized.

For the Cr 3d states, the initial orbital degeneracy is lifted by the crystal field splitting and spin−orbit coupling. The crystal field in the trigonal prismatic geometry splits the states into three energy levels, d_{z^2}, ($d_{x^2-y^2}/d_{xy}$), and (d_{yz}/d_{xz}), with increasing energy (*cf.* level diagram in Figure 6b) and well-defined magnetic quantum numbers of m_l = 0, ±2, and ±1, respectively. These levels correspond to the irreducible representations a_1', e′, and e″ of the D_{3h} point symmetry group. Upon including SOC the remaining degeneracy is further reduced. Because SOC is proportional to the angular momentum operator times the spin operator $\hat{L}_z\hat{S}_z$, atomic orbitals with a nonvanishing magnetic quantum number ($m_l \neq 0$) split into new eigenstates of the total angular momentum operator $\hat{J}$.

This qualitative picture can be quantitatively described by our fully relativistic, noncollinear DFT calculations. The orbital character of the Cr_W impurity states is obtained by projection onto atomic orbitals as shown in Figure 6d. As described above, we find three defect states associated with Cr 3d orbitals that have predominantly d_{z^2}, ($d_{x^2-y^2}/d_{xy}$), and (d_{yz}/d_{xz}) character, corresponding to the crystal field splitting. Including SOC the three defect states split into five states. Projections of the Cr_W DOS with SOC onto eigenstates of the total angular momentum operator reveal that the three states in the band gap (formerly denoted I, IIa, and IIb) are mainly composed of $m_j = \pm 1/2, \pm 3/2, \pm 5/2$ components. The two higher states in the WS_2 conduction band are mixtures of $m_j = \pm 1/2$ and $\pm 3/2$, where j and m_j denote the expectation value for $\hat{J}$ and $\hat{J}_z$, respectively (see Figure 6b,f). The spin−orbit splitting between IIa and IIb was calculated to be 48 meV, which is close to the experimental value of 80 meV.

It should be noted that the Cr_W defect states are hybrid orbitals with contributions from Cr 3d, W 5d, and S 3p states (see Figure S12). Hence, the intuitive atomistic view underlying the defect−molecule model is limited. However, it is justified for deep in-gap states where orbital overlap is small. The electronic character of Cr_W defect states is different from that of a S vacancy that is mainly composed of W 5d. The orbital contributions of Cr's 3d electrons effectively reduce the spin−orbit splitting of Cr_W as compared to Vac_S.

The deep, spin−orbit split defect states observed for Cr_W impurities and sulfur vacancies[22] offer several qualities that are of potential interest for solid-state photonic spin qubits. Their discrete states are well decoupled from dispersive bulk states, they are accessible and tunable by virtue of the two-dimensionality of the host crystal, and they can be coupled to electric fields *via* SOC.[84] Recently, it was suggested that defect complexes of chalcogen vacancies and paramagnetic impurities such as rhenium can act as ideal two-level systems with emission in the telecom wavelength range.[15] Our findings for Cr_W suggest that the targeted incorporation of such paramagentic impurities is feasible in a standard CVD process by controlling the impurity levels of the precursors. While chalcogen vacancies are not present in our as-grown samples,[25] they can be generated by thermal annealing.[22] Alternatively, defects could be introduced site-selectively *via* ion-beam irradiation[36,85] or atomic manipulation.

Defect−Defect Interaction: Cr_W Dimer. Defect−defect interactions become relevant as the mean defect separation becomes comparable to the dimension of the defect orbitals. In our samples we can consider most point defects as isolated. However, we find occasions where two defects are in close proximity such that defect states hybridize. In Figure 7, a Cr_W dimer in a third-nearest-neighbor configuration is shown. The dI/dV spectra across the dimer (Figure 7d,e) reveal a substantial hybridization between the Cr_W in-gap states. The number of hybrid states formed is difficult to assess, as the defect resonances significantly overlap. Six identifiable peaks are indicated by the dashed lines in Figure 7e. The original three Cr_W states (arrows in Figure 7e) fall within the range of the hybrid states, consistent with the notion of bonding and antibonding hybrid states.

For the same Cr_W dimer geometry we calculated the band structure with DFT in a 7 × 7 supercell as shown in Figure 7g,h. For both with (Figure 7h) and without (Figure 7g) considering SOC, we find six Cr_W dimer states. These nondegenerate states result from the lower crystal field symmetry, as compared to an isolated Cr_W, and orbital hybridization between the two Cr impurities. The relative energies of these hybrid orbitals with respect to the three isolated Cr impurity states are in quantitative agreement with experiment.

When approaching higher Cr doping densities toward the formation of a $Cr_xW_{1-x}S_2$ alloy, we expect that a dispersive defect band will form in the same energy range. Defect state hybridization was only observed for two equivalent defects. Hybrid dimers without orbital energy overlap such as Cr_WMo_W or Cr_WO_S did not form mixed states.

Isoelectronic Trap States Due to d Shell Energetics and Strain: Cr_W *vs* Mo_W. In the sections Chromium Substituting Tungsten (Cr_W) and Molybdenum Substituting Tungsten (Mo_W) we described the formation of deep in-gap states for chromium substituting tungsten (Cr_W) and their absence for molybdenum substituting tungsten (Mo_W). Next we discuss possible reasons for the different behavior of these isoelectronic substitutions.

Cr, Mo, and W are all group VI transition metals. However, unlike W, Cr and Mo are exceptions of the Aufbau principle with the following electron configurations: Cr: [Ar] $3d^5 4s^1$, Mo: [Kr] $4d^5 5s^1$, W: [Xe] $5d^4 6s^2$. In other aspects like their coordination

DOI: 10.1021/acsnano.9b04611
ACS Nano 2019, 13, 10520−10534

chemistry Mo and W are more alike than Cr. This is reflected in the abundance of certain oxidation states. For Mo and W, the +6 oxidation state prevails, whereas for Cr the lower +3 oxidation state is most abundant. For instance, the most stable W and Mo oxides are WO_3 and MO_3, whereas Cr forms Cr_2O_3.[86]

Furthermore, the metallic radius of Cr (128 pm[87]) is considerably smaller than that of both Mo (139 pm[87]) and W (139 pm[87]). This is reflected in the observed local strain around the Cr substituent. In Figure 8c–f we compare the sulfur–sulfur distance in the top sulfur plane determined from the experimental nc-AFM images and nc-AFM simulations using an atom fitting routine (Atomap[88]). For both the experiment and simulation, we observe a reduced distance between the three surface sulfur atoms closest to the Cr substituent (white triangle in Figure 8c,e). The apparent distance between the three sulfur atoms in the CO-tip nc-AFM image and simulation is slightly smaller than their actual geometric distance. This can be explained by the well-known CO-tip tilting,[89] which effectively enhances the relaxation effect. The simulations that are based on the probe particle model[67,68] account for the CO-tip tilting and yield a 6% change in the sulfur–sulfur distance like observed experimentally. The DFT-calculated defect geometry (shown in Figure 8a) that serves as an input for the nc-AFM simulation shows a 4.5% reduction [as mentioned in the section Molybdenum Substituting Tungsten (Mo_W)]. Hence, we can use the scaling factor between the DFT geometry and the simulated nc-AFM image to calibrate the effective lattice strain, indicated by the right colorbar in Figure 8c–f. For Mo_W no detectable strain was observed.

Lastly, the different energetics of the Cr 3d states and the Mo 4d states are discussed. In TMDs the states close to the valence and conduction band are made of transition metal d electrons and chalcogen p electrons. The degree of hybridization and the energetic location of the hybrid states depend on the level alignment between these d and p electrons. In Figure 8g,h we plot the projected density of states of WS_2 with a W substitution onto the substituent's d orbitals. We find that for Mo_W the valence band and conduction band edge comprise Mo's d_{z^2}, $d_{x^2-y^2}$, and d_{xy} states, as in the nondefective case. For Cr_W in contrast, d_{z^2}, $d_{x^2-y^2}$, and d_{xy} contribute to a lesser extent to the valence band but completely unmix in the unoccupied density of states, creating the Cr_W in-gap defect states, as discussed in detail in the section Spin–Orbit Splitting of Cr_W Defect States.

The qualitatively different behavior of the isoelectronic substitutes Cr and Mo in WS_2, in particular the isoelectronic trap states introduced by Cr_W, can therefore be rationalized by two main effects: Cr's smaller atomic radius that leads to local strain and the different energetics of 3d *vs* 4d orbitals. These differences are similarly reflected in the different coordination chemistry of group VI transition metals.

Tight-Binding Model for Localizing Isoelectronic Substitutes. Above, we have shown that DFT calculations can accurately describe structural and electronic properties of point defects in monolayer WS_2. We now compare our DFT results to tight-binding (TB) models that have been used as an alternative approach to describe TMD electronic properties. As we discussed earlier, the d_{xz} and d_{yz} orbitals are pushed far away from the band gap region due to crystal field splitting in the D_{3h} point group symmetry.[32] Thus, the basic electronic characteristics of monolayer TMD such as the direct band gap at the K point and the spin–valley coupling can be obtained by considering a minimal basis consisting of the three transition metal d orbitals (d_{xy}, $d_{x^2-y^2}$, and d_{z^2}) that have even parity with respect to the σ_h symmetry plane of the crystal.[90] For point defects, which in general reduce the symmetry of the crystal structure, induce local atomic distortions, and create a different chemical environment, the basis set has to be extended to include also d_{xz} and d_{yz} orbitals in order to predict the correct energy spectrum. For instance, the electronic structure of monolayer TMDs with transition metal or chalcogen vacancies has been calculated in the framework of a six-band TB model, which differs from that obtained by an 11-band TB model.[28,33] The latter can describe the electronic structure of actual vacancies and gives a good agreement with our DFT calculations for both *actual* W and S vacancies (see Figures S14 and S15). Intriguingly, the electronic structure of W and S vacancies in the framework of the *six-band* TB model resembles DFT calculations for Cr_W and O_S very well (see Figure 9), meaning that the vacancies in the six-band TB model effectively represent the electronic spectrum of isoelectronic substitutions as opposed to actual vacancy defects. The vacancies in the six-band TB model can be regarded as the limiting case of a zero hopping integral and infinite onsite energy at the defect site. This suggests that Cr and O substituents strongly localize electrons in the vicinity of their atomic site.

This may come from the fact that covalently bonded isoelectronic substitutes restore the crystal structure to a certain extent, such that the Hamiltonian can be approximately decoupled into even and odd parts, just like for pristine TMDs. Hence, a smaller basis set of just even orbitals may suffice. Depending on the type of substitute, the degree of hybridization with its neighboring atoms can vary substantially. Mo_W represents a case of strong hybridization (supporting extended Bloch states), which essentially restores the WS_2 band structure [*cf.* the section Molybdenum Substituting Tungsten (Mo_W)]. Cr_W and O_S represent cases of strong electron localization, simulated by describing them as "vacancies" in the reduced six-band TB model.

Work Function Change at CD-Rich Domains. While most of the charged defects are usually randomly distributed (like all other defects), in some samples we observe CD-rich

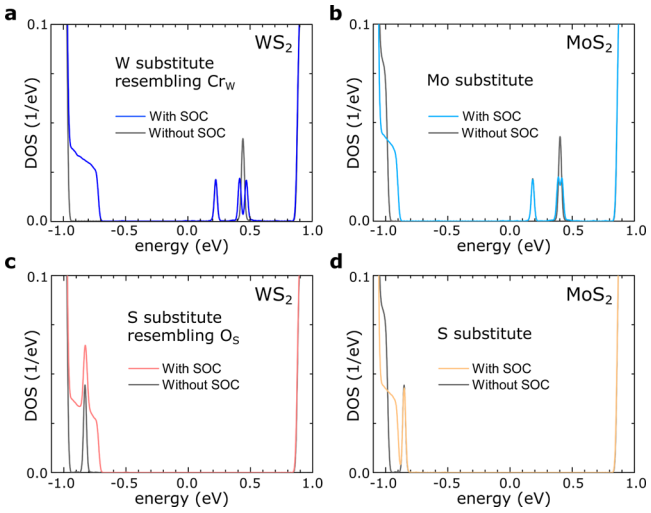

Figure 9. Tight-binding model for localizing transition metal and chalcogen substitutions. (a, b) Calculated DOS for a localizing W substitution and S substitution in WS_2 with and without SOC. (e, f) Calculated DOS for a localizing Mo substitution and S substitution in MoS_2 with and without SOC.

DOI: 10.1021/acsnano.9b04611
ACS Nano 2019, 13, 10520–10534

domains with a very high CD density. In Figure 10a–c, a CD segregated domain is shown. Such domains are at least a few 100 nm in size. The transition from a pristine WS_2 area with a normal defect density to the highly defective CD-rich area occurs over about 20 nm. Figure 10a,b display such a transition area. Just as for a single CD we find a bias-dependent contrast inversion originating from the upward band bending (*cf.* the section Charged Defects (CD) Type I and Type II).

Using KPFS we study the work function difference between the pristine and highly defective regions. KPFS measurements across a domain boundary (blue arrow in Figure 10c) are shown in Figure 10d. While on the pristine WS_2 an LCPD of about −0.2 V is measured, the LCPD is significantly increased to about 0.9 V in the CD-rich region. This striking increase of the work function by 1.1 V at the CD-rich domain is a consequence of the bound negative charge at CD defects.

The reason for the formation of CD-rich domains in certain samples is not known. The segregation of CD defects might be thermodynamically favorable at higher CD densities, or extended domains only form in a certain growth temperature regime. So far unexplored is also whether these domains are located in a specific location of WS_2 islands, such as island edges or centers.[91]

CONCLUSIONS

In summary, we identified and characterized the observed point defects in CVD-grown monolayer WS_2 using a combination of low-temperature STM/STS, CO-tip nc-AFM, Kelvin probe force spectroscopy, and DFT calculations. The defects' characteristic electronic fingerprint enables an unambiguous defect assignment and reveals their optoelectronic functionality. We found two tungsten substitutions, Cr_W and Mo_W, and three sulfur substitutions, O_S in the top and bottom sulfur layer and one type of charged defect. Sulfur vacancies were not observed in as-grown samples but could be generated by high-temperature annealing under vacuum.[22]

Cr_W forms three deep, unoccupied defect states. Two of these states arise from spin–orbit coupling as observed by STM orbital imaging and corroborated by DFT calculations. The formation of isoelectronic trap states of Cr_W is in contrast to Mo_W, which does not form localized in-gap states. This strikingly different behavior results from the different energetics of Cr's 3d *vs* Mo's 4d electrons as well as lattice strain. The local strain field was directly mapped by CO-tip nc-AFM images. In addition, the defect electronic structure of both Cr_W and O_S can be explained by a stronger binding of electrons at these isoelectronic substituents as described by a simple tight-binding model. While most other defects are randomly distributed and can be considered isolated, we find some cases of interacting defects that form hybrid defect orbitals as exemplified by a Cr_W dimer.

At two types of CDs, we observe a strong upward band bending and increase of the local contact potential difference indicative of the localization of negative charge. Some samples were found to feature CD-rich domains of a few hundred nanometers in size that lead to a significant work function increase.

The deep in-gap defect states of Cr_W and the negative charge localization at CDs are highly relevant for the transport and optical properties of WS_2. Both will act as effective radiative recombination centers and might host defect-bound excitons. The negatively charged CDs are also expected to strongly scatter charge carriers and potentially trap excitons to form localized

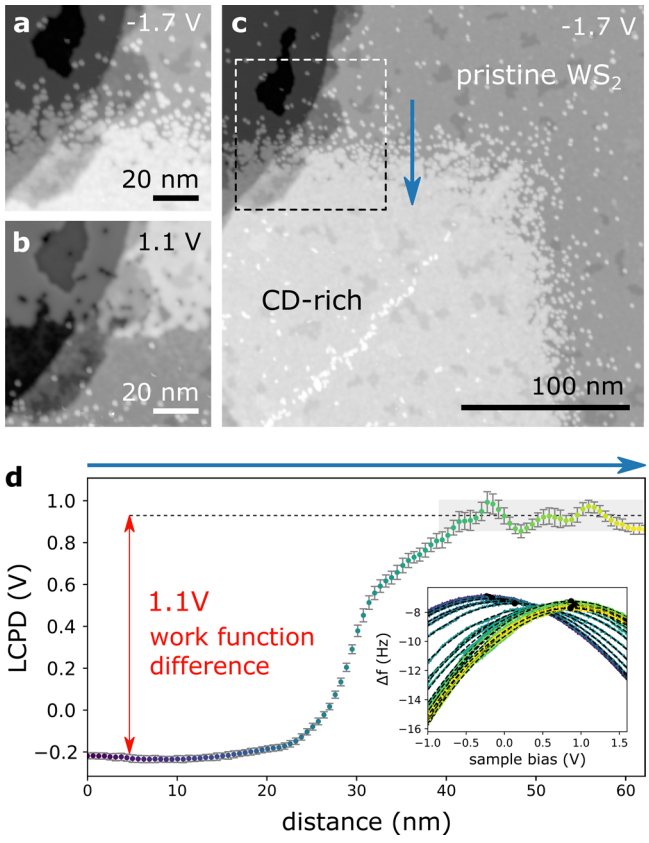

Figure 10. Large work function shift in CD-rich domain. (a, b) STM topography at −1.7 and 1.1 V, respectively, of a domain boundary separating pristine WS_2 from a highly defective region with many CD defects (bottom part). The bias-dependent contrast inversion is also observed for a single CD. (c) Larger STM overview image of the same WS_2 island. The dashed box indicates the scan area displayed in a and b. (d) Kelvin probe force spectroscopy (KPFS) across the CD-rich domain boundary indicated by the blue arrow in c. The shift in the local contact potential difference (LCPD) reveals the large work function difference of 1.1 V between the pristine WS_2 and the CD-rich area. The inset shows a subset of KPFM parabolas from which the LCPD was extracted.

trions. The defect properties reported here will guide future efforts of targeted defect engineering and doping of TMDs.

METHODS

WS_2/MLG/SiC Growth Procedure. WS_2 few-layer islands were grown by a modified chemical vapor deposition process[57] on graphitized (6H)-SiC substrates.[92] We used $WO_{2.9}$ powder (99.99%, Alfa Aesar) and H_2S gas as the metal and chalcogen precursors, respectively. The samples were not deliberately doped. The growth temperature was 900 °C, and the growth time was 1 h. Further details can be found in the Supporting Information.

Scanning Probe Measurements. *Setup.* The experiments were performed using a CreaTec low-temperature ($T \approx 6$ K), ultrahigh vacuum ($p \approx 10^{-10}$ mbar) combined STM and AFM. The sensor was based on a qPlus[93] quartz-crystal cantilever design operated in the frequency-modulation mode[94] (resonance frequency $f_0 \approx 30$ kHz, spring constant $k \approx 1800$ N/m, quality factor $Q \approx 30\,000$, and oscillation amplitude $A \approx 1$ Å). The voltage was applied to the sample. STM images were taken in constant-current mode at $I = 10–100$ pA and $V = 1.1$ V if not stated otherwise. STS spectra are performed in constant-height mode with a lock-in amplifier with a frequency of 670 Hz and 5 mV amplitude. The STS spectra have been characterized on Au(111) to ensure a flat tip density of states. AFM measurements were acquired in constant-height mode at $V = 0$ V.

DOI: 10.1021/acsnano.9b04611
ACS Nano 2019, 13, 10520–10534

Sample and Tip Preparation. The CVD-grown WS_2/Gr/SiC was annealed *in vacuo* at about 250 °C for 30 min. We used focused ion beam cut PtIr tips or chemically etched W tips that were sharpened by repeated indentations into a Au substrate. A CO tip was created by picking up a single CO molecule from the Au(111) surface.[62,63] Both the Au(111) and the WS_2/Gr/SiC were mounted on the same sample holder.

Density-Functional Theory Calculations. We performed first-principles DFT calculations using Quantum-Espresso.[95,96] We used the PBE generalized gradient approximation[97] for the exchange–correlation functional with scalar and fully relativistic optimized norm-conserving Vanderbilt (ONCV) pseudopotentials from Pseudo-Dojo library.[98] We used the experimental lattice parameter of 3.15 Å[99] and a 5 × 5 or 7 × 7 WS_2 supercell with a ∼15 Å vacuum region. We applied a plane wave cutoff energy of 100 Ry and 4 × 4 × 1 (3 × 3) *k*-point sampling for a 5 × 5 (7 × 7) supercell. We simulated the orbital character by means of integrated local density of states. More details on the effect of the DFT functional and lattice constant can be found in the Supporting Information.

Tight-Binding Model. The tight-binding calculations are implemented following ref 28. We consider single layers of WS_2 containing 2400 × 2400 atoms, with periodic boundary conditions. The electronic band structure is considered from a tight-binding model that contains six-bands: three W 5d orbitals (d_{xy}, $d_{x^2-y^2}$, and d_{z^2}) and three S 3p orbitals (p_x, p_y, and p_z).[100] Intra-atomic spin–orbit coupling is included in the model. The density of states and quasi-eigenstates are obtained numerically from the tight-binding propagation method.[101] In the simulations, localizing substitutions are mimicked by randomly removing sulfur or tungsten atoms without lattice relaxation. More details on the tight-binding model can be found in the Supporting Information.

ASSOCIATED CONTENT

Supporting Information

The Supporting Information is available free of charge on the ACS Publications website at DOI: 10.1021/acsnano.9b04611.

CVD growth details of WS_2 on Gr/SiC, lattice site identification for Mo_W and CD type II, CO-tip nc-AFM simulations of WS_2 defects, DFT calculations of other substitutional defects considered, details on the tight-binding calculations (PDF)

AUTHOR INFORMATION

Corresponding Authors

*E-mail: bschuler@lbl.gov.
*E-mail: junholee@lbl.gov.
*E-mail: jbneaton@lbl.gov.

ORCID

Bruno Schuler: 0000-0002-9641-0340
Christoph Kastl: 0000-0001-5309-618X
Katherine A. Cochrane: 0000-0001-8268-2938
Sivan Refaely-Abramson: 0000-0002-7031-8327
Nicholas J. Borys: 0000-0001-5434-1191
Roland J. Koch: 0000-0001-5748-8463
Adam M. Schwartzberg: 0000-0001-6335-0719

Notes

The authors declare no competing financial interest.

ACKNOWLEDGMENTS

We would like to thank Thomas Seyller for help preparing the graphene on SiC substrates and Prokop Hapala for support with setting up the AFM simulations. This work was performed at the Molecular Foundry supported by the Office of Science, Office of Basic Energy Sciences, of the U.S. Department of Energy under Contract No. DE-AC02-05CH11231. B.S. appreciates support from the Swiss National Science Foundation under project number P2SKP2_171770. J.-H.L. and J.B.N. were supported by the Theory FWP, which is funded by the Department of Energy, Office of Science, Basic Energy Sciences, Materials Sciences and Engineering Division, under Contract No. DE-AC02-05CH11231. C.K. gratefully acknowledges support by the Bavaria California Technology Center (BaCaTeC) and the International Graduate School of Science and Engineering (IGSSE) through project "CommOnChip". A.W.-B. was supported by the U.S. Department of Energy Early Career Award. S.Y. acknowledges the financial support by the National Key R&D Program of China (Grant No. 2018FYA0305800) and computational resources provided by the Supercomputing Center of Wuhan University.

REFERENCES

(1) Lin, Z.; Carvalho, B. R.; Kahn, E.; Lv, R.; Rao, R.; Terrones, H.; Pimenta, M. A.; Terrones, M. Defect Engineering of Two-Dimensional Transition Metal Dichalcogenides. *2D Mater.* **2016**, *3*, 022002.

(2) Novoselov, K.; Mishchenko, A.; Carvalho, A.; Neto, A. C. 2D Materials and Van Der Waals Heterostructures. *Science* **2016**, *353*, aac9439.

(3) Manzeli, S.; Ovchinnikov, D.; Pasquier, D.; Yazyev, O. V.; Kis, A. 2D Transition Metal Dichalcogenides. *Nat. Rev. Mater.* **2017**, *2*, 17033.

(4) Mak, K. F.; Shan, J. Photonics and Optoelectronics of 2D Semiconductor Transition Metal Dichalcogenides. *Nat. Photonics* **2016**, *10*, 216.

(5) Das, S.; Robinson, J. A.; Dubey, M.; Terrones, H.; Terrones, M. Beyond Graphene: Progress in Novel Two-Dimensional Materials and Van Der Waals Solids. *Annu. Rev. Mater. Res.* **2015**, *45*, 1–27.

(6) Li, Y.; Chernikov, A.; Zhang, X.; Rigosi, A.; Hill, H. M.; van der Zande, A. M.; Chenet, D. A.; Shih, E.-M.; Hone, J.; Heinz, T. F. Measurement of the Optical Dielectric Function of Monolayer Transition-Metal Dichalcogenides: MoS_2, $MoSe_2$, WS_2, and WSe_2. *Phys. Rev. B: Condens. Matter Mater. Phys.* **2014**, *90*, 205422.

(7) Xu, X.; Yao, W.; Xiao, D.; Heinz, T. F. Spin and Pseudospins in Layered Transition Metal Dichalcogenides. *Nat. Phys.* **2014**, *10*, 343.

(8) Schaibley, J. R.; Yu, H.; Clark, G.; Rivera, P.; Ross, J. S.; Seyler, K. L.; Yao, W.; Xu, X. Valleytronics in 2D Materials. *Nat. Rev. Mater.* **2016**, *1*, 16055.

(9) Zhu, Z.; Cheng, Y.; Schwingenschlögl, U. Giant Spin-Orbit-Induced Spin Splitting in Two-Dimensional Transition-Metal Dichalcogenide Semiconductors. *Phys. Rev. B: Condens. Matter Mater. Phys.* **2011**, *84*, 153402.

(10) Ugeda, M. M.; Bradley, A. J.; Shi, S.-F.; Felipe, H.; Zhang, Y.; Qiu, D. Y.; Ruan, W.; Mo, S.-K.; Hussain, Z.; Shen, Z.-X.; et al. Giant Bandgap Renormalization and Excitonic Effects in a Monolayer Transition Metal Dichalcogenide Semiconductor. *Nat. Mater.* **2014**, *13*, 1091–1095.

(11) Yao, K.; Yan, A.; Kahn, S.; Suslu, A.; Liang, Y.; Barnard, E. S.; Tongay, S.; Zettl, A.; Borys, N. J.; Schuck, P. J. Optically Discriminating Carrier-Induced Quasiparticle Band Gap and Exciton Energy Renormalization in Monolayer MoS_2. *Phys. Rev. Lett.* **2017**, *119*, 087401.

(12) Qiu, D. Y.; da Jornada, F. H.; Louie, S. G. Optical Spectrum of MoS_2: Many-body Effects and Diversity of Exciton States. *Phys. Rev. Lett.* **2013**, *111*, 216805.

(13) Yang, J.-H.; Yakobson, B. Dimensionality-Suppressed Chemical Doping in 2D Semiconductors: The Cases of Phosphorene, MoS_2, and ReS_2 from First-Principles. *arXiv:1711.05094*, **2017**.

(14) Aharonovich, I.; Englund, D.; Toth, M. Solid-State Single-Photon Emitters. *Nat. Photonics* **2016**, *10*, 631.

(15) Gupta, S.; Yang, J.-H.; Yakobson, B. I. Two-Level Quantum Systems in Two-Dimensional Materials for Single Photon Emission. *Nano Lett.* **2019**, *19*, 408.

DOI: 10.1021/acsnano.9b04611
ACS Nano 2019, 13, 10520–10534

(16) Zhou, W.; Zou, X.; Najmaei, S.; Liu, Z.; Shi, Y.; Kong, J.; Lou, J.; Ajayan, P. M.; Yakobson, B. I.; Idrobo, J.-C. Intrinsic Structural 16. Defects in Monolayer Molybdenum Disulfide. *Nano Lett.* **2013**, *13*, 2615−2622.
(17) Barja, S.; Wickenburg, S.; Liu, Z.-F.; Zhang, Y.; Ryu, H.; Ugeda, M. M.; Hussain, Z.; Shen, Z.-X.; Mo, S.-K.; Wong, E.; et al. Charge Density Wave Order in 1D Mirror Twin Boundaries of Single-Layer $MoSe_2$. *Nat. Phys.* **2016**, *12*, 751−756.
(18) Wang, S.; Robertson, A.; Warner, J. H. Atomic Structure of Defects and Dopants in 2D Layered Transition Metal Dichalcogenides. *Chem. Soc. Rev.* **2018**, *47*, 6764−6794.
(19) Lin, Y.-C.; Björkman, T.; Komsa, H.-P.; Teng, P.-Y.; Yeh, C.-H.; Huang, F.-S.; Lin, K.-H.; Jadczak, J.; Huang, Y.-S.; Chiu, P.-W.; et al. Three-Fold Rotational Defects in Two-Dimensional Transition Metal Dichalcogenides. *Nat. Commun.* **2015**, *6*, 6736.
(20) Komsa, H.-P.; Kotakoski, J.; Kurasch, S.; Lehtinen, O.; Kaiser, U.; Krasheninnikov, A. V. Two-Dimensional Transition Metal Dichalcogenides Under Electron Irradiation: Defect Production and Doping. *Phys. Rev. Lett.* **2012**, *109*, 035503.
(21) Klein, J.; Kuc, A.; Nolinder, A.; Altzschner, M.; Wierzbowski, J.; Sigger, F.; Kreupl, F.; Finley, J.; Wurstbauer, U.; Holleitner, A.; et al. Robust Valley Polarization of Helium Ion Modified Atomically Thin MoS_2. *2D Mater.* **2018**, *5*, 011007.
(22) Schuler, B.; Qiu, D. Y.; Refaely-Abramson, S.; Kastl, C.; Chen, C. T.; Barja, S.; Koch, R. J.; Ogletree, D. F.; Aloni, S.; Schwartzberg, A. M.; et al. Large Spin-Orbit Splitting of Deep In-Gap Defect States of Engineered Sulfur Vacancies in Monolayer WS_2. *Phys. Rev. Lett.* **2019**, *123*, 076801.
(23) Hildebrand, B.; Didiot, C.; Novello, A. M.; Monney, G.; Scarfato, A.; Ubaldini, A.; Berger, H.; Bowler, D.; Renner, C.; Aebi, P. Doping Nature of Native Defects in 1T-$TiSe_2$. *Phys. Rev. Lett.* **2014**, *112*, 197001.
(24) Gao, J.; Kim, Y. D.; Liang, L.; Idrobo, J. C.; Chow, P.; Tan, J.; Li, B.; Li, L.; Sumpter, B. G.; Lu, T.-M.; et al. Transition-Metal Substitution Doping in Synthetic Atomically Thin Semiconductors. *Adv. Mater.* **2016**, *28*, 9735−9743.
(25) Barja, S.; Refaely-Abramson, S.; Schuler, B.; Qiu, D. Y.; Pulkin, A.; Wickenburg, S.; Ryu, H.; Ugeda, M. M.; Kastl, C.; Chen, C.; et al. Identifying Substitutional Oxygen as a Prolific Point Defect in Monolayer Transition Metal Dichalcogenides with Experiment and Theory. *Nat. Commun.* **2019**, *10*, 3382.
(26) Van Der Zande, A. M.; Huang, P. Y.; Chenet, D. A.; Berkelbach, T. C.; You, Y.; Lee, G.-H.; Heinz, T. F.; Reichman, D. R.; Muller, D. A.; Hone, J. C. Grains and Grain Boundaries in Highly Crystalline Monolayer Molybdenum Disulphide. *Nat. Mater.* **2013**, *12*, 554−561.
(27) Le, D.; Rahman, T. S. Joined Edges in MoS_2: Metallic and Half-Metallic Wires. *J. Phys.: Condens. Matter* **2013**, *25*, 312201.
(28) Yuan, S.; Roldán, R.; Katsnelson, M.; Guinea, F. Effect of Point Defects on the Optical and Transport Properties of MoS_2 and WS_2. *Phys. Rev. B: Condens. Matter Mater. Phys.* **2014**, *90*, 041402.
(29) Lehtinen, O.; Komsa, H.-P.; Pulkin, A.; Whitwick, M. B.; Chen, M.-W.; Lehnert, T.; Mohn, M. J.; Yazyev, O. V.; Kis, A.; Kaiser, U.; et al. Atomic Scale Microstructure and Properties of Se-Deficient Two-Dimensional $MoSe_2$. *ACS Nano* **2015**, *9*, 3274−3283.
(30) Komsa, H.-P.; Krasheninnikov, A. V. Native Defects in Bulk and Monolayer MoS_2 from First Principles. *Phys. Rev. B: Condens. Matter Mater. Phys.* **2015**, *91*, 125304.
(31) Haldar, S.; Vovusha, H.; Yadav, M. K.; Eriksson, O.; Sanyal, B. Systematic Study of Structural, Electronic, and Optical Properties of Atomic-Scale Defects in the Two-Dimensional Transition Metal Dichalcogenides MX_2 (M= Mo, W; X= S, Se, Te). *Phys. Rev. B: Condens. Matter Mater. Phys.* **2015**, *92*, 235408.
(32) Li, W.-F.; Fang, C.; van Huis, M. A. Strong Spin-Orbit Splitting and Magnetism of Point Defect States in Monolayer WS_2. *Phys. Rev. B: Condens. Matter Mater. Phys.* **2016**, *94*, 195425.
(33) Khan, M.; Erementchouk, M.; Hendrickson, J.; Leuenberger, M. N. Electronic and Optical Properties of Vacancy Defects in Single-Layer Transition Metal Dichalcogenides. *Phys. Rev. B: Condens. Matter Mater. Phys.* **2017**, *95*, 245435.
(34) Naik, M. H.; Jain, M. Substrate Screening Effects on the Quasiparticle Band Gap and Defect Charge Transition Levels in MoS_2. *Phys. Rev. Materials* **2018**, *2*, 084002.
(35) Qiu, H.; Xu, T.; Wang, Z.; Ren, W.; Nan, H.; Ni, Z.; Chen, Q.; Yuan, S.; Miao, F.; Song, F.; et al. Hopping Transport Through Defect-Induced Localized States in Molybdenum Disulphide. *Nat. Commun.* **2013**, *4*, 2642.
(36) Tongay, S.; Suh, J.; Ataca, C.; Fan, W.; Luce, A.; Kang, J. S.; Liu, J.; Ko, C.; Raghunathanan, R.; Zhou, J.; et al. Defects Activated Photoluminescence in Two-Dimensional Semiconductors: Interplay Between Bound, Charged, and Free Excitons. *Sci. Rep.* **2013**, *3*, 2657.
(37) Chow, P. K.; Jacobs-Gedrim, R. B.; Gao, J.; Lu, T.-M.; Yu, B.; Terrones, H.; Koratkar, N. Defect-Induced Photoluminescence in Monolayer Semiconducting Transition Metal Dichalcogenides. *ACS Nano* **2015**, *9*, 1520−1527.
(38) Carozo, V.; Wang, Y.; Fujisawa, K.; Carvalho, B. R.; McCreary, A.; Feng, S.; Lin, Z.; Zhou, C.; Perea-López, N.; Elías, A. L.; et al. Optical Identification of Sulfur Vacancies: Bound Excitons at the Edges of Monolayer Tungsten Disulfide. *Sci. Adv.* **2017**, *3*, No. e1602813.
(39) Saigal, N.; Ghosh, S. Evidence for Two Distinct Defect Related Luminescence Features in Monolayer MoS_2. *Appl. Phys. Lett.* **2016**, *109*, 122105.
(40) He, Y.-M.; Clark, G.; Schaibley, J. R.; He, Y.; Chen, M.-C.; Wei, Y.-J.; Ding, X.; Zhang, Q.; Yao, W.; Xu, X.; et al. Single Quantum Emitters in Monolayer Semiconductors. *Nat. Nanotechnol.* **2015**, *10*, 497−502.
(41) Chakraborty, C.; Kinnischtzke, L.; Goodfellow, K. M.; Beams, R.; Vamivakas, A. N. Voltage-Controlled Quantum Light from an Atomically Thin Semiconductor. *Nat. Nanotechnol.* **2015**, *10*, 507−511.
(42) Koperski, M.; Nogajewski, K.; Arora, A.; Cherkez, V.; Mallet, P.; Veuillen, J.-Y.; Marcus, J.; Kossacki, P.; Potemski, M. Single Photon Emitters in Exfoliated WSe_2 Structures. *Nat. Nanotechnol.* **2015**, *10*, 503−506.
(43) Srivastava, A.; Sidler, M.; Allain, A. V.; Lembke, D. S.; Kis, A.; Imamoğlu, A. Optically Active Quantum Dots in Monolayer WSe_2. *Nat. Nanotechnol.* **2015**, *10*, 491−496.
(44) Li, G.; Zhang, D.; Qiao, Q.; Yu, Y.; Peterson, D.; Zafar, A.; Kumar, R.; Curtarolo, S.; Hunte, F.; Shannon, S.; et al. All the Catalytic Active Sites of MoS_2 for Hydrogen Evolution. *J. Am. Chem. Soc.* **2016**, *138*, 16632−16638.
(45) Li, H.; Tsai, C.; Koh, A. L.; Cai, L.; Contryman, A. W.; Fragapane, A. H.; Zhao, J.; Han, H. S.; Manoharan, H. C.; Abild-Pedersen, F.; et al. Activating and Optimizing MoS_2 Basal Planes for Hydrogen Evolution Through the Formation of Strained Sulphur Vacancies. *Nat. Mater.* **2016**, *15*, 48.
(46) Hong, J.; Jin, C.; Yuan, J.; Zhang, Z. Atomic Defects in Two-Dimensional Materials: From Single-Atom Spectroscopy to Functionalities in Opto-/Electronics, Nanomagnetism, and Catalysis. *Adv. Mater.* **2017**, *29*, 1606434
(47) Zhang, W.; Li, X.; Jiang, T.; Song, J.; Lin, Y.; Zhu, L.; Xu, X. CVD Synthesis of $Mo_{1-x}W_xS_2$ and $MoS_{2(1-x)}Se_{2x}$ Alloy Monolayers Aimed at Tuning the Bandgap of Molybdenum Disulfide. *Nanoscale* **2015**, *7*, 13554−13560.
(48) Zhang, M.; Wu, J.; Zhu, Y.; Dumcenco, D. O.; Hong, J.; Mao, N.; Deng, S.; Chen, Y.; Yang, Y.; Jin, C.; et al. Two-Dimensional Molybdenum Tungsten Diselenide Alloys: Photoluminescence, Raman Scattering, and Electrical Transport. *ACS Nano* **2014**, *8*, 7130−7137.
(49) Tongay, S.; Narang, D. S.; Kang, J.; Fan, W.; Ko, C.; Luce, A. V.; Wang, K. X.; Suh, J.; Patel, K.; Pathak, V.; et al. Two-Dimensional Semiconductor Alloys: Monolayer $Mo_{1-x}W_xSe_2$. *Appl. Phys. Lett.* **2014**, *104*, 012101.
(50) Suh, J.; Tan, T. L.; Zhao, W.; Park, J.; Lin, D.-Y.; Park, T.-E.; Kim, J.; Jin, C.; Saigal, N.; Ghosh, S.; et al. Reconfiguring Crystal and Electronic Structures of MoS_2 by Substitutional Doping. *Nat. Commun.* **2018**, *9*, 199.
(51) Hong, J.; Hu, Z.; Probert, M.; Li, K.; Lv, D.; Yang, X.; Gu, L.; Mao, N.; Feng, Q.; Xie, L.; et al. Exploring Atomic Defects in Molybdenum Disulphide Monolayers. *Nat. Commun.* **2015**, *6*, 6293.

DOI: 10.1021/acsnano.9b04611
ACS Nano 2019, 13, 10520−10534

(52) Liu, X.; Balla, I.; Bergeron, H.; Hersam, M. C. Point Defects and Grain Boundaries in Rotationally Commensurate MoS_2 on Epitaxial Graphene. *J. Phys. Chem. C* **2016**, *120*, 20798−20805.
(53) Zhang, S.; Wang, C.-G.; Li, M.-Y.; Huang, D.; Li, L.-J.; Ji, W.; Wu, S. Defect Structure of Localized Excitons in a WSe_2 Monolayer. *Phys. Rev. Lett.* **2017**, *119*, 046101.
(54) Lin, Y.-C.; Jariwala, B.; Bersch, B. M.; Xu, K.; Nie, Y.; Wang, B.; Eichfeld, S. M.; Zhang, X.; Choudhury, T. H.; Pan, Y.; et al. Realizing Large-Scale, Electronic-Grade Two-Dimensional Semiconductors. *ACS Nano* **2018**, *12*, 965−975.
(55) Kobayashi, Y.; Sasaki, S.; Mori, S.; Hibino, H.; Liu, Z.; Watanabe, K.; Taniguchi, T.; Suenaga, K.; Maniwa, Y.; Miyata, Y. Growth and Optical Properties of High-Quality Monolayer WS_2 on Graphite. *ACS Nano* **2015**, *9*, 4056−4063.
(56) Forti, S.; Rossi, A.; Büch, H.; Cavallucci, T.; Bisio, F.; Sala, A.; Menteş, T. O.; Locatelli, A.; Magnozzi, M.; Canepa, M.; et al. Electronic Properties of Single-Layer Tungsten Disulfide on Epitaxial Graphene on Silicon Carbide. *Nanoscale* **2017**, *9*, 16412.
(57) Kastl, C.; Chen, C.; Koch, R. J.; Schuler, B.; Kuykendall, T.; Bostwick, A.; Jozwiak, C.; Seyller, T.; Rotenberg, E.; Weber-Bargioni, A.; et al. Multimodal Spectromicroscopy of Monolayer WS_2 Enabled by Ultra-Clean van der Waals Epitaxy. *2D Mater.* **2018**, *5*, 045010.
(58) Kastl, C.; Chen, C. T.; Kuykendall, T.; Shevitski, B.; Darlington, T. P.; Borys, N. J.; Krayev, A.; Schuck, P. J.; Aloni, S.; Schwartzberg, A. M. The Important Role of Water in Growth of Monolayer Transition Metal Dichalcogenides. *2D Mater.* **2017**, *4*, 021024.
(59) Ulstrup, S.; Giusca, C. E.; Miwa, J. A.; Sanders, C. E.; Browning, A.; Dudin, P.; Cacho, C.; Kazakova, O.; Gaskill, D. K.; Myers-Ward, R. L.; et al. Nanoscale Mapping of Quasiparticle Band Alignment. *Nat. Commun.* **2019**, *10*, 3283.
(60) Riedl, C.; Coletti, C.; Iwasaki, T.; Zakharov, A.; Starke, U. Quasi-Free-Standing Epitaxial Graphene on SiC Obtained by Hydrogen Intercalation. *Phys. Rev. Lett.* **2009**, *103*, 246804.
(61) Park, J. H.; Vishwanath, S.; Liu, X.; Zhou, H.; Eichfeld, S. M.; Fullerton-Shirey, S. K.; Robinson, J. A.; Feenstra, R. M.; Furdyna, J.; Jena, D.; et al. Scanning Tunneling Microscopy and Spectroscopy of Air Exposure Effects on Molecular Beam Epitaxy Grown WSe_2 Monolayers and Bilayers. *ACS Nano* **2016**, *10*, 4258−4267.
(62) Gross, L.; Mohn, F.; Moll, N.; Liljeroth, P.; Meyer, G. The Chemical Structure of a Molecule Resolved by Atomic Force Microscopy. *Science* **2009**, *325*, 1110.
(63) Mohn, F.; Schuler, B.; Gross, L.; Meyer, G. Different Tips for High-Resolution AFM and STM Imaging of Single Molecules. *Appl. Phys. Lett.* **2013**, *102*, 073109.
(64) Sánchez-Sánchez, C.; González, C.; Jelinek, P.; Méndez, J.; De Andres, P.; Martín-Gago, J. A.; López, M. F. Understanding Atomic-Resolved STM Images on TiO_2(110)-(1× 1) Surface by DFT Calculations. *Nanotechnology* **2010**, *21*, 405702.
(65) Tumino, F.; Casari, C. S.; Passoni, M.; Russo, V.; Bassi, A. L. Pulsed Laser Deposition of Single-Layer MoS_2 on Au(111): From Nanosized Crystals to Large-Area Films. *Nanoscale Adv.*. **2019**, *1*, 643.
(66) Moll, N.; Gross, L.; Mohn, F.; Curioni, A.; Meyer, G. The Mechanisms Underlying the Enhanced Resolution of Atomic Force Microscopy with Functionalized Tips. *New J. Phys.* **2010**, *12*, 125020.
(67) Hapala, P.; Kichin, G.; Wagner, C.; Tautz, F. S.; Temirov, R.; Jelínek, P. Mechanism of High-Resolution STM/AFM Imaging with Functionalized Tips. *Phys. Rev. B: Condens. Matter Mater. Phys.* **2014**, *90*, 085421.
(68) Hapala, P.; Temirov, R.; Tautz, F. S.; Jelínek, P. Origin of High-Resolution IETS-STM Images of Organic Molecules with Functionalized Tips. *Phys. Rev. Lett.* **2014**, *113*, 226101.
(69) Robertson, A. W.; Lin, Y.-C.; Wang, S.; Sawada, H.; Allen, C. S.; Chen, Q.; Lee, S.; Lee, G.-D.; Lee, J.; Han, S.; et al. Atomic Structure and Spectroscopy of Single Metal (Cr, V) Substitutional Dopants in Monolayer MoS_2. *ACS Nano* **2016**, *10*, 10227−10236.
(70) Karthikeyan, J.; Komsa, H.-P.; Batzill, M.; Krasheninnikov, A. V. Which Transition Metal Atoms Can Be Embedded Into Two-Dimensional Molybdenum Dichalcogenides and Add Magnetism? *Nano Lett.* **2019**, *19*, 4581.
(71) Le Quang, T.; Nogajewski, K.; Potemski, M.; Dau, M. T.; Jamet, M.; Mallet, P.; Veuillen, J. Band-Bending Induced by Charged Defects and Edges of Atomically Thin Transition Metal Dichalcogenide Films. *2D Mater.* **2018**, *5*, 035034.
(72) Addou, R.; Colombo, L.; Wallace, R. M. Surface Defects on Natural MoS_2. *ACS Appl. Mater. Interfaces* **2015**, *7*, 11921−11929.
(73) Mohn, F.; Gross, L.; Moll, N.; Meyer, G. Imaging the Charge Distribution Within a Single Molecule. *Nat. Nanotechnol.* **2012**, *7*, 227.
(74) Gross, L.; Mohn, F.; Liljeroth, P.; Repp, J.; Giessibl, F. J.; Meyer, G. Measuring the Charge State of an Adatom with Noncontact Atomic Force Microscopy. *Science* **2009**, *324*, 1428.
(75) Aghajanian, M.; Mostofi, A. A.; Lischner, J. Tuning Electronic Properties of Transition-Metal Dichalcogenides via Defect Charge. *Sci. Rep.* **2018**, *8*, 13611.
(76) Schulz, F.; Ijäs, M.; Drost, R.; Hämäläinen, S. K.; Harju, A.; Seitsonen, A. P.; Liljeroth, P. Many-Body Transitions in a Single Molecule Visualized by Scanning Tunnelling Microscopy. *Nat. Phys.* **2015**, *11*, 229.
(77) Yu, P.; Kocić, N.; Repp, J.; Siegert, B.; Donarini, A. Apparent Reversal of Molecular Orbitals Reveals Entanglement. *Phys. Rev. Lett.* **2017**, *119*, 056801.
(78) Schoenaers, B.; Stesmans, A.; Afanas'ev, V. V. Nitrogen Acceptor in 2H-Polytype Synthetic MoS_2 Assessed by Multifrequency Electron Spin Resonance. *J. Vac. Sci. Technol., A* **2018**, *36*, 05G503.
(79) Azcatl, A.; Qin, X.; Prakash, A.; Zhang, C.; Cheng, L.; Wang, Q.; Lu, N.; Kim, M. J.; Kim, J.; Cho, K.; et al. Covalent Nitrogen Doping and Compressive Strain in MoS_2 by Remote N_2 Plasma Exposure. *Nano Lett.* **2016**, *16*, 5437−5443.
(80) Tang, B.; Yu, Z. G.; Huang, L.; Chai, J.; Wong, S. L.; Deng, J.; Yang, W.; Gong, H.; Wang, S.; Ang, K.-W.; et al. Direct *n*- to *p*-Type Channel Conversion in Monolayer/Few-Layer WS_2 Field-Effect Transistors by Atomic Nitrogen Treatment. *ACS Nano* **2018**, *12*, 2506−2513.
(81) Zhang, F.; Lu, Y.; Schulman, D. S.; Zhang, T.; Fujisawa, K.; Lin, Z.; Lei, Y.; Elias, A. L.; Das, S.; Sinnott, S. B.; et al. Carbon Doping of WS_2 Monolayers: Bandgap Reduction and *p*-Type Doping Transport. *Sci. Adv.* **2019**, *5*, No. eaav5003.
(82) Mak, K. F.; He, K.; Shan, J.; Heinz, T. F. Control of Valley Polarization in Monolayer MoS_2 by Optical Helicity. *Nat. Nanotechnol.* **2012**, *7*, 494.
(83) Coulson, C. A.; Kearsley, M. J. Colour Centres in Irradiated Diamonds. I. *Proc. R. Soc. London A* **1957**, *241*, 433−454.
(84) van der Heijden, J.; Kobayashi, T.; House, M. G.; Salfi, J.; Barraud, S.; Laviéville, R.; Simmons, M. Y.; Rogge, S. Readout and Control of the Spin-Orbit States of Two Coupled Acceptor Atoms in a Silicon Transistor. *Sci. Adv.* **2018**, *4*, No. eaat9199.
(85) Klein, J.; Lorke, M.; Florian, M.; Sigger, F.; Sigl, L.; Rey, S.; Wierzbowski, J.; Cerne, J.; Müller, K.; Mitterreiter, E.; et al. Site-Selectively Generated Photon Emitters in Monolayer MoS_2 Via Local Helium Ion Irradiation. *Nat. Commun.* **2019**, *10*, 2755.
(86) Fierro, J., Ed. *Metal Oxides*, 1st ed.; CRC Press, 2005.
(87) Greenwood, N. N.; Earnshaw, A. *Chemistry of the Elements*, 2nd ed.; Elsevier, 2012.
(88) Nord, M.; Vullum, P. E.; MacLaren, I.; Tybell, T.; Holmestad, R. Atomap: A New Software Tool for the Automated Analysis of Atomic Resolution Images Using Two-Dimensional Gaussian Fitting. *Adv. Struct. Chem. Imaging* **2017**, *3*, 9.
(89) Gross, L.; Mohn, F.; Moll, N.; Schuler, B.; Criado, A.; Guitián, E.; Peña, D.; Gourdon, A.; Meyer, G. Bond-Order Discrimination by Atomic Force Microscopy. *Science* **2012**, *337*, 1326.
(90) Xiao, D.; Liu, G.-B.; Feng, W.; Xu, X.; Yao, W. Coupled Spin and Valley Physics in Monolayers of MoS_2 and Other Group-VI Dichalcogenides. *Phys. Rev. Lett.* **2012**, *108*, 196802.
(91) Bao, W.; Borys, N. J.; Ko, C.; Suh, J.; Fan, W.; Thron, A.; Zhang, Y.; Buyanin, A.; Zhang, J.; Cabrini, S.; et al. Visualizing Nanoscale Excitonic Relaxation Properties of Disordered Edges and Grain Boundaries in Monolayer Molybdenum Disulfide. *Nat. Commun.* **2015**, *6*, 7993.

DOI: 10.1021/acsnano.9b04611
ACS Nano 2019, 13, 10520−10534

(92) Emtsev, K. V.; Bostwick, A.; Horn, K.; Jobst, J.; Kellogg, G. L.; Ley, L.; McChesney, J. L.; Ohta, T.; Reshanov, S. A.; Röhrl, J.; et al. Towards Wafer-Size Graphene Layers by Atmospheric Pressure Graphitization of Silicon Carbide. *Nat. Mater.* **2009**, *8*, 203.
(93) Giessibl, F. J. High-Speed Force Sensor for Force Microscopy and Profilometry Utilizing a Quartz Tuning Fork. *Appl. Phys. Lett.* **1998**, *73*, 3956.
(94) Albrecht, T. R.; Grütter, P.; Horne, D.; Rugar, D. Frequency Modulation Detection Using High-Q Cantilevers for Enhanced Force Microscope Sensitivity. *J. Appl. Phys.* **1991**, *69*, 668−673.
(95) Giannozzi, P.; Baroni, S.; Bonini, N.; Calandra, M.; Car, R.; Cavazzoni, C.; Ceresoli, D.; Chiarotti, G. L.; Cococcioni, M.; Dabo, I.; et al. QUANTUM ESPRESSO: A Modular and Open-Source Software Project for Quantum Simulations of Materials. *J. Phys.: Condens. Matter* **2009**, *21*, 395502.
(96) Giannozzi, P.; Andreussi, O.; Brumme, T.; Bunau, O.; Nardelli, M. B.; Calandra, M.; Car, R.; Cavazzoni, C.; Ceresoli, D.; Cococcioni, M.; et al. Advanced Capabilities for Materials Modelling with Quantum ESPRESSO. *J. Phys.: Condens. Matter* **2017**, *29*, 465901.
(97) Perdew, J. P.; Burke, K.; Ernzerhof, M. Generalized Gradient Approximation Made Simple. *Phys. Rev. Lett.* **1996**, *77*, 3865−3868.
(98) Hamann, D. R. Optimized Norm-Conserving Vanderbilt Pseudopotentials. *Phys. Rev. B: Condens. Matter Mater. Phys.* **2013**, *88*, 085117.
(99) Schutte, W.; De Boer, J.; Jellinek, F. Crystal Structures of Tungsten Disulfide and Diselenide. *J. Solid State Chem.* **1987**, *70*, 207−209.
(100) Cappelluti, E.; Roldán, R.; Silva-Guillén, J. A.; Ordejón, P.; Guinea, F. Tight-Binding Model and Direct-Gap/Indirect-Gap Transition in Single-Layer and Multilayer MoS_2. *Phys. Rev. B: Condens. Matter Mater. Phys.* **2013**, *88*, 075409.
(101) Yuan, S.; De Raedt, H.; Katsnelson, M. I. Modeling Electronic Structure and Transport Properties of Graphene with Resonant Scattering Centers. *Phys. Rev. B: Condens. Matter Mater. Phys.* **2010**, *82*, 115448.

DOI: 10.1021/acsnano.9b04611
ACS Nano 2019, 13, 10520−10534